Mon. Not. R. Astron. Soc. **323**, 188–210 (2001)

Modelling gaseous and stellar kinematics in the disc galaxies NGC 772, 3898 and 7782

E. Pignatelli,[1★] E. M. Corsini,[2] J. C. Vega Beltrán,[3] C. Scarlata,[4] A. Pizzella,[2] J. G. Funes S. J.,[5] W. W. Zeilinger,[6] J. E. Beckman[3] and F. Bertola[4]

[1]*SISSA, via Beirut 2-4, I-34013 Trieste, Italy*
[2]*Osservatorio Astrofisico di Asiago, Dipartimento di Astronomia, Università di Padova, via dell'Osservatorio 8, I-36012 Asiago, Italy*
[3]*Instituto Astrofísico de Canarias, Calle Via Lactea s/n, E-38200 La Laguna, Spain*
[4]*Dipartimento di Astronomia, Università di Padova, vicolo dell'Osservatorio 5, I-35122 Padova, Italy*
[5]*Vatican Observatory, University of Arizona, Tucson, AZ 85721, USA*
[6]*Institut für Astronomie, Universität Wien, Türkenschanzstraße 17, A-1180 Wien, Austria*

Accepted 2000 November 13. Received 2000 November 9; in original form 2000 September 6

ABSTRACT

We present *V*-band surface photometry and major-axis kinematics of stars and ionized gas of three early-type spiral galaxies, namely NGC 772, 3898 and 7782. For each galaxy we present a self-consistent Jeans model for the stellar kinematics, adopting the light distribution of bulge and disc derived by means of a two-dimensional parametric photometric decomposition. This allows us to investigate the presence of non-circular gas motions, and derive the mass distribution of luminous and dark matter in these objects.

NGC 772 and 7782 have apparently normal kinematics with the ionized gas tracing the gravitational equilibrium circular speed. This is not true in the innermost region ($|r| \leq$ 8 arcsec) of NGC 3898, where the ionized gas is rotating more slowly than the circular velocity predicted by dynamical modelling. This phenomenon is common in the bulge-dominated galaxies for which dynamical modelling enables us to make the direct comparison between the gas velocity and the circular speed, and it poses questions about the reliability of galaxy mass distributions derived by the direct decomposition of the observed ionized-gas rotation curve into the contributions of luminous and dark matter.

Key words: galaxies: formation – galaxies: kinematics and dynamics – galaxies: spiral – galaxies: structure.

1 INTRODUCTION

In the past, kinematic and dynamical studies of disc galaxies have been mainly focused on late-type spirals. With respect to lenticular and early-type spiral galaxies (defined as those with $B/T > 0.3$, following Simien & de Vaucouleurs 1986), the study of late-type spirals has many advantages from both the observational and the interpretative points of view. Late-type spirals have small or even negligible bulges, so they are usually described as luminous discs embedded in dark matter haloes. They are on average more gas-rich than early-type spirals. Gas is mainly confined to the galactic disc, considered to be moving at circular speed and therefore used as direct tracer of the gravitational potential. Since the line-of-sight velocity distribution (LOSVD hereafter) of ionized or neutral hydrogen is easier to measure than the stellar one, the number of spirals of known gaseous kinematics increased faster than that of the galaxies for which stellar motions were measured. These facts made late-type spirals easy targets, particularly in the search for dark matter (see Sofue & Rubin 2001 for a review).

Only recently, Heraudeau & Simien (1998) and Heraudeau et al. (1999) measured the stellar rotation curves and velocity-dispersion profiles along the major axis of a large sample of spirals (more than 60 objects) ranging from Sa to Sc. In last few years, systematic surveys have been started to derive the stellar and gaseous kinematics in S0 galaxies (Bertola et al. 1995; Bettoni & Galletta 1997; Fisher 1997) and in early-to-intermediate-type spirals (Corsini et al. 1999; Vega Beltrán 1999; Vega Beltrán et al., in preparation).

If the direct comparison of stellar and gaseous kinematics allowed to unveil also in disc galaxies the presence of kinematically decoupled components (see Bertola & Corsini 1999 for a recent review), the application of dynamical models showed that in the bulge-dominated region the ionized-gas velocity may fall below the circular speed (Fillmore, Boroson & Dressler 1986; Kent 1988; Kormendy & Westpfahl 1989). These

★ E-mail: pignatel@sissa.it

'slowly rising' rotation curves have been interpreted as the signature of the presence of pressure-supported gas (Bertola et al. 1995; Cinzano et al. 1999), which has been recently expelled by stars of the bulge but not yet heated to the virial temperature of the galaxy. This discovery poses new questions about the reliability of galaxy mass distributions derived by the decomposition of the observed ionized-gas rotation curve into the contributions of luminous and dark matter. In fact, the inner gradient of the gas velocity curve is usually used to fix the amount of luminous matter, which results to be underestimated if gas velocity rises slowly than circular speed.

In this paper we present a study of the ionized-gas and stellar kinematics for three Sa – Sb galaxies, namely NGC 772, 3898 and 7782. We apply a self-consistent dynamical model based on a two-dimensional photometric decomposition method to explain the different kinematical behaviour of gas and stars. The goal of this work is to derive the mass distribution of these objects and investigate the possible presence of non-circular gas motions in the bulge region.

The paper is organized as it follows. In Section 2 we give an overview of the properties of NGC 772, 3898 and 7782; in Section 3 we present the broad- and narrow-band imaging and major-axis kinematics of stars and ionized gas; in Section 4 we discuss the photometric and dynamical techniques adopted to investigate the light and mass distribution of these galaxies; in Section 5 we apply these techniques to the galaxies, deriving their structural and kinematic parameters; finally, Section 6 is devoted to a discussion of the results, and our conclusions.

2 GLOBAL PROPERTIES OF NGC 772, 3898 AND 7782

The galaxies studied in this paper are a subset of the 20 disc galaxies observed by Vega Beltrán et al. (in preparation). All these galaxies are bright ($B_T \leq 13.5$) and nearby objects ($V_\odot < 5800\,\mathrm{km\,s^{-1}}$) with intermediate-to-high inclinations ($i \geq 45°$), and their Hubble morphological types run from S0 to Sc.

Since the presence of ionized gas supported by non-circular motions has been observed only in lenticular or bulge-dominated spiral galaxies, we focused our attention on S0 – Sb galaxies. We selected unbarred galaxies according to the classification of both Sandage & Tammann (1981, hereafter RSA) and de Vaucouleurs et al. (1991, hereafter RC3). To better disentangle the contributions of the bulge, the disc and eventually of the dark matter halo to the total mass of the galaxy, we choose among the sample objects those with the more extended ionized-gas and stellar kinematics (in units of R_{25}). At the end of this selection process we remained with five galaxies: an S0 (NGC 980), two Sa (NGC 772 and 5064) and two Sb spirals (NGC 3898 and 7782).

All the selected galaxies display a smooth and regular morphology, except for NGC 772 which is characterized by a strong lopsidedness (Fig. 6). However, the symmetry of velocity curves and velocity-dispersion profiles of both ionized gas and stars (Fig. 2) suggests us that also NGC 772 has an axisymmetric structure, at least in the radial region where the kinematic parameters were measured (corresponding to $0.2R_{25}$).

An accurate analysis of the photometric and kinematic properties of the selected galaxies (see Vega Beltràn 1999 for details) showed that the surface brightness of NGC 980 is characterized by a strong twisting of the isophotes, and that the LOSVD profiles of NGC 5064 have a strongly non-Gaussian shape. We interpreted these two phenomena as due to the misalignment between bulge and disc of NGC 980 (or even to the presence of a triaxial bulge) and to the possible coexistence in NGC 5064 of two counter-rotating components, respectively. Therefore the two galaxies were discarded and are not studied here.

An overview of the properties of the remaining galaxies, namely NGC 772, 3898 and 7782 which will be the subject of our investigation, is given in Table 1. Their available photometric and kinematical data are listed here briefly.

Table 1. Optical and radio properties of NGC 772, 3898 and 7782.

Parameter	NGC 772	NGC 3898	NGC 7782
Other name	UGC 1466; PGC 7525	UGC 6787; PGC 36921	UGC 12834; PGC 72788
Morphological type	Sb(rs)I[a]; Sb[b]; SAS3[c]	SaI[a]; Sa[b]; SAS2[c]	Sb(s)I–II[a]; Sb[b]; SAS3[c]
Heliocentric systemic velocity ($\mathrm{km\,s^{-1}}$)[d]	2470 ± 10	1184 ± 10	5430 ± 10
Distance (Mpc)[d]	34.7	17.1	75.2
Major-axis position angle[c]	130°	107°	175°
Apparent isophotal diameters[c]	7.2×4.3	4.4×2.6	2.4×1.3
Inclination[d]	54°	54°	58°
Apparent V_T magnitude (mag)[c]	10.31	10.70	12.23
Total $(B-V)_T$ colour index (mag)[c]	0.78	0.90	0.85
Total corrected V luminosity $L_{V_T^0}$ ($L_{\odot,V}$)[d]	11.2×10^{10}	1.6×10^{10}	9.7×10^{10}
H I linewidth at 20% of the peak ($\mathrm{km\,s^{-1}}$)	473[e]	504[f]	570[g]
H I linewidth at 50% of the peak ($\mathrm{km\,s^{-1}}$)	410[e]	469[f]	559[g]
Mass of neutral hydrogen $M_{\mathrm{H\,I}}$ ($M_\odot$)	25.6×10^{9}[e]	2.6×10^{9}[f]	14.5×10^{9}[g]
Mass of cool dust M_d ($M_\odot$)[h]	2.3×10^{7}	0.07×10^{7}	2.3×10^{7}

[a] from RSA.
[b] from Nilson (1973, hereafter UGC).
[c] from RC3. The apparent isophotal diameters are measured at a surface brightness level of $\mu_B = 25\,\mathrm{mag\,arcsec^{-2}}$.
[d] from this paper. The distance is derived as V_0/H_0 with V_0 the velocity relative to the centroid of the Local Group obtained from the heliocentric systemic velocity as in RSA and $H_0 = 75\,\mathrm{km\,s^{-1}\,Mpc^{-1}}$. The inclination i is derived as $\cos^2 i = (q^2 - q_0^2)/(1 - q_0^2)$, where the observed axial ratio is taken from RC3 and an intrinsic flattening of $q_0 = 0.11$ has been assumed, following Guthrie (1992).
[e] from Rhee & van Albada (1996). The neutral hydrogen mass has been scaled for the adopted distance.
[f] from van Driel & van Woerden (1994). The neutral hydrogen mass has been scaled for the adopted distance.
[g] from Krumm & Salpeter (1980). The neutral hydrogen mass has been scaled for the adopted distance.
[h] derived following Young et al. (1989) from the IRAS flux densities at 60 and 100 μm (Moshir et al. 1990).

2.1 NGC 772

Surface photometry of NGC 772 was obtained in the *B* band by Lu (1998), who also derived the photometric parameters of the exponential disc, and in the *V* and *I* bands by Heraudeau & Simien (1996). NGC 772 belongs to the sample of 34 early-to-late spiral galaxies, whose major-axis stellar velocities have been recently measured by Heraudeau & Simien (1998). NGC 772 was observed in the 21-cm line of neutral hydrogen by Rhee & van Albada (1996), who obtained the H I position–velocity map, global velocity profile and radial surface density distribution. These data show the asymmetric distribution of the H I at radii larger than 5 armin from the centre. On the NW side a low rotation-velocity ($V_{\rm H\,I} \simeq 100\,{\rm km\,s^{-1}}$) component can be traced out to 9 arcmin, while on the SE the H I emission extends to 5 arcmin with a rotation velocity of $260\,{\rm km\,s^{-1}}$.

2.2 NGC 3898

Surface photometry of NGC 3898 is available in *B* (Barbon, Benacchio & Capaccioli 1978; Boroson 1981), *V* (Watanabe 1983; Kodaira, Okamura & Ichikawa 1990; Heraudeau & Simien 1996), *I* (Heraudeau & Simien 1996), *r* (Kent 1988), *J* (Giovanardi & Hunt 1996; Moriondo, Giovanardi & Hunt 1998a), *H* (Giovanardi & Hunt 1996), and *K* band (Giovanardi & Hunt 1996; Moriondo et al. 1998a). Whitmore, Rubin & Ford (1984), Fillmore et al. (1986) and Heraudeau et al. (1999) measured the major-axis stellar velocity curve and velocity-dispersion profile of NGC 3898. The ionized-gas rotation curve was obtained along the galaxy major axis by Rubin et al. (1985) and Fillmore et al. (1986). The distribution and velocity field of H I were studied in detail by van Driel & van Woerden (1994), who also derived, using the maximum-disc hypothesis (van Albada & Sancisi 1986), the mass contribution of bulge, disc and dark halo by fitting the combined Hα/H I rotation curve using the photometric parameters of bulge and disc obtained from Watanabe's (1983) surface-brightness profile. Other mass models for NGC 3898 have been obtained by Fillmore et al. (1986), using both gas and stellar kinematics, and by Kent (1988) and Moriondo, Giovanardi & Hunt (1998b), who adopted the ionized-gas kinematics by Rubin et al. (1985).

2.3 NGC 7782

Surface photometry of NGC 7782 has been obtained in the *V* band (Kodaira et al. 1990), the *r* band (Courteau 1996) and the *H* band (Moriondo et al. 1999). The only available bulge–disc decomposition for NGC 7782 is that of Baggett, Baggett & Anderson (1998) based on the data of Kodaira et al. (1990). No spatially resolved kinematics for the gaseous and stellar components have been obtained for this galaxy either at optical or at radio wavelengths.

3 OBSERVATIONS AND DATA REDUCTION

3.1 Long-slit spectroscopy

The spectroscopic observations of NGC 772, 3898 and 7782 were carried out in two different runs during 1990 October and December at the 4.5-m Multiple Mirror Telescope (MMT) on Mt. Hopkins (Arizona, USA). The $1200\,{\rm groove\,mm^{-1}}$ grating blazed at 5767 Å was used in the first order in combination with a 1.25 arcsec × 3.0 arcmin slit and the Loral 1200 × 800 CCD with pixels of $15 \times 15\,\mu{\rm m}^2$. It yielded a wavelength coverage of 650 Å between 4850 and 5500 Å, with a reciprocal dispersion of $54.7\,{\rm Å\,mm^{-1}}$. No on-chip binning was performed and every spectrum pixel corresponded to 0.82 Å by 0.30 arcsec.

Table 2. Log of the spectroscopic observations.

Object	Date	Telescope	$t_{\rm exp}$ [s]	PA [°]
NGC 772	22 Oct 1990	MMT	3600	130
NGC 3898	18 Dec 1990	MMT	3600	107
	19 Mar 1996	INT	4 × 3600	107
NGC 7782	22 Oct 1990	MMT	3600	175

NGC 3898 was also observed at the Isaac Newton Telescope (INT) in La Palma (Spain) on 1996 March 19. The Intermediate Dispersion Spectrograph (IDS) was used with a 1.9 arcsec × 4.0 arcmin slit, the 500-mm camera, the AgRed collimator, and the H1800V grating with $1800\,{\rm groove\,mm^{-1}}$ at first order. This instrumental set-up yielded a wavelength coverage of 240 Å between 6650 and 6890 Å, with a reciprocal dispersion of $9.92\,{\rm Å\,mm^{-1}}$. No on-chip binning was applied on the adopted 1024×1024 TK1024A CCD. Each $24 \times 24\,\mu{\rm m}^2$ spectrum pixel corresponds to 0.24 Å by 0.33 arcsec.

At the beginning of each exposure, the slit was centred on the galaxy nucleus using the guiding TV camera and aligned along the galaxy major axis. The details on the slit position and spectra exposure times are given in Table 2. At the MMT, spectra of a number of late-G and early-K giant stars were obtained with the same set-up to serve as templates in measuring the stellar kinematics. In all observing runs, comparison exposures of the arc lamp were taken before and after each object integration to allow an accurate wavelength calibration. Quartz-lamp and twilight-sky flat-fields were used to map pixel-to-pixel sensitivity variations and large-scale illumination patterns. The seeing during the observations was typically between 1.2 and 1.5 arcsec FWHM.

Using standard MIDAS[1] routines the spectra were bias-subtracted, flat-field-corrected and wavelength-calibrated. Cosmic rays were identified by comparing the counts in each pixel with the local mean and standard deviation (as obtained by the Poisson statistics of the photons knowing the gain and readout noise of the detector), and corrected by interpolating. The instrumental resolution was derived by measuring the Gaussian FWHM of a dozen of unblended arc-lamp lines distributed over the whole spectral range of a wavelength-calibrated comparison spectrum. We found a mean value of FWHM = 2.24 ± 0.26 Å and of FWHM = 2.57 ± 0.11 Å for the MMT spectra obtained in 1990 October and December, respectively. They correspond to instrumental velocity dispersions of $\sigma_{\rm instr} = 55$ and $64\,{\rm km\,s^{-1}}$ at 5150 Å. For the INT spectra we measured a mean FWHM = 0.87 ± 0.04 Å that, in the range of the observed gas emission lines, corresponds to an instrumental velocity dispersion of $\sigma_{\rm instr} = 17\,{\rm km\,s^{-1}}$.

The stellar kinematic parameters were measured from the absorption lines present on MMT spectra using the Fourier Correlation Quotient method (Bender 1990), as applied by Bender, Saglia & Gerhard (1994). The spectra of the G5III star HR 7778 and the K2III star HR 6415 provided the best match to galaxy spectra obtained in 1990 October and December, respectively, so they were used as templates to measure the galaxy stellar velocities in the two runs. The stellar kinematics of NGC 772,

[1] MIDAS is developed and maintained by the European Southern Observatory.

Table 3. Stellar kinematics along the major axis of NGC 772.

r [″] (1)	V [km s^{-1}] (2)	δV (3)	σ [km s^{-1}] (4)	$\delta\sigma$ (5)	h_3 (6)	δh_3 (7)	h_4 (8)	δh_4 (9)
−24.1	2650	12	64	2	−0.48	0.05	−0.56	0.05
−10.4	2596	12	115	17	−0.03	0.07	0.08	0.07
−5.2	2557	12	110	12	−0.01	0.06	0.06	0.06
−3.0	2542	12	86	1	0.05	0.01	0.18	0.01
−1.9	2525	12	62	2	0.06	0.01	0.37	0.01
−1.1	2514	12	109	7	−0.07	0.04	0.02	0.04
−0.5	2501	12	114	7	−0.05	0.05	−0.02	0.05
0.1	2475	12	116	8	0.06	0.04	0.05	0.04
0.6	2458	12	112	15	0.07	0.08	0.04	0.08
1.4	2443	12	113	1	0.03	0.01	0.02	0.01
2.5	2401	12	79	2	0.15	0.01	0.22	0.01
4.6	2400	12	120	13	0.07	0.06	0.06	0.06
8.7	2378	12	122	14	0.06	0.07	0.05	0.07
25.7	2343	12	68	30	0.04	0.06	0.84	0.06

Table 4. Stellar kinematics along the major axis of NGC 3898.

r [″] (1)	V [km s^{-1}] (2)	δV (3)	σ [km s^{-1}] (4)	$\delta\sigma$ (5)	h_3 (6)	δh_3 (7)	h_4 (8)	δh_4 (9)
−30.8	1300	12	121	13	0.05	0.03	0.43	0.03
−18.2	1296	26	138	33	0.06	0.17	0.01	0.17
−14.5	1306	44	127	26	−0.03	0.30	−0.17	0.30
−12.3	1325	26	131	17	−0.15	0.17	−0.09	0.17
−10.6	1315	31	119	20	−0.19	0.22	−0.09	0.22
−9.3	1312	31	127	41	−0.04	0.21	0.02	0.21
−8.9	1308	17	129	15	−0.06	0.11	−0.05	0.11
−6.6	1291	12	154	14	−0.10	0.07	0.00	0.07
−5.1	1278	23	162	22	−0.01	0.12	−0.04	0.12
−4.1	1262	15	175	21	−0.04	0.08	0.03	0.08
−3.3	1233	17	185	20	0.00	0.08	−0.00	0.08
−2.7	1243	12	189	14	−0.03	0.06	−0.01	0.06
−2.1	1224	12	214	14	0.00	0.04	0.03	0.04
−1.7	1216	18	203	29	0.03	0.08	0.07	0.08
−1.4	1206	18	228	25	−0.01	0.07	0.02	0.07
−1.1	1220	12	240	17	0.02	0.04	0.04	0.04
−0.8	1197	12	229	11	0.05	0.03	0.02	0.03
−0.5	1197	12	218	13	0.00	0.04	0.03	0.04
−0.2	1186	12	230	15	0.01	0.05	0.01	0.05
0.1	1187	12	219	15	0.01	0.05	0.01	0.05
0.4	1172	12	227	12	0.01	0.03	0.02	0.03
0.7	1153	12	240	11	0.02	0.03	0.03	0.03
1.0	1144	12	228	14	0.05	0.05	−0.01	0.05
1.3	1141	12	221	15	0.00	0.05	0.02	0.05
1.6	1149	12	221	13	0.05	0.04	0.04	0.04
2.1	1126	12	208	13	0.01	0.04	0.01	0.04
2.7	1114	16	200	22	−0.02	0.07	0.03	0.07
3.3	1100	12	201	16	0.04	0.05	0.04	0.05
4.0	1109	14	187	20	0.04	0.06	0.04	0.06
5.0	1097	12	178	9	0.06	0.05	−0.04	0.05
6.7	1078	12	182	15	0.05	0.06	0.01	0.06
9.2	1058	14	156	16	0.10	0.08	−0.01	0.08
10.8	1041	27	153	35	0.19	0.15	0.02	0.15
12.2	1047	35	144	35	−0.03	0.21	−0.03	0.21
14.3	1068	26	162	28	0.06	0.14	−0.02	0.14
17.6	1066	36	134	38	0.08	0.23	−0.02	0.23

3898 and 7782 are discussed in Sections 5.1.1, 5.2.1 and 5.3.1, and the key parameters are tabulated in Tables 3–5. Each table provides the radial distance from the galaxy centre in arcsec, the observed heliocentric velocity and velocity dispersion in km s^{-1}, and the Gauss–Hermite coefficients h_3 and h_4.

The ionized-gas kinematics were derived by measuring the position and width of the [O III] λ5006.8 and Hα emission lines in the MMT and INT spectra, respectively. Using the MIDAS package

Table 5. Stellar kinematics along the major axis of NGC 7782.

r [″] (1)	V [km s^{-1}] (2)	δV (3)	σ [km s^{-1}] (4)	$\delta\sigma$ (5)	h_3 (6)	δh_3 (7)	h_4 (8)	δh_4 (9)
−39.0	5187	12	9	7	−0.27	0.25	0.23	0.25
−33.5	5184	12	34	1	−0.08	0.08	−0.39	0.08
−28.8	5199	12	42	3	0.18	0.10	−0.14	0.10
−24.8	5189	12	39	2	−0.01	0.08	−0.13	0.08
−20.7	5173	12	6	0	0.00	0.08	0.00	0.08
−18.4	5179	12	69	11	−0.21	0.09	0.06	0.09
−16.8	5178	12	98	14	−0.33	0.08	0.07	0.08
−15.1	5184	12	70	7	0.17	0.08	−0.01	0.08
−13.5	5168	12	64	3	0.29	0.07	−0.16	0.07
−12.0	5228	12	82	58	0.17	0.10	0.77	0.10
−10.6	5245	12	121	18	−0.39	0.09	0.05	0.09
−9.4	5225	12	118	7	−0.05	0.09	−0.30	0.09
−7.3	5268	12	110	23	0.30	0.09	0.12	0.09
−5.8	5216	12	73	27	0.73	0.09	0.36	0.09
−4.6	5264	12	99	4	0.24	0.07	−0.24	0.07
−3.3	5319	12	148	5	0.01	0.05	−0.23	0.05
−2.5	5339	14	182	14	0.10	0.07	−0.04	0.07
−1.9	5334	14	178	9	0.10	0.07	−0.09	0.07
−1.5	5334	14	144	23	0.19	0.09	0.07	0.09
−1.2	5341	19	177	11	0.24	0.09	−0.15	0.09
−0.9	5343	12	129	22	0.17	0.07	0.14	0.07
−0.6	5387	13	169	9	0.00	0.07	−0.09	0.07
−0.3	5393	12	159	7	0.18	0.07	−0.15	0.07
0.0	5426	14	192	8	0.09	0.06	−0.11	0.06
0.3	5474	12	122	33	−0.11	0.08	0.29	0.08
0.6	5441	13	163	12	−0.03	0.07	−0.04	0.07
0.9	5483	12	141	12	−0.11	0.06	0.00	0.06
1.2	5488	18	179	26	−0.22	0.09	0.04	0.09
1.7	5501	12	174	13	0.02	0.06	−0.02	0.06
2.3	5492	12	158	11	0.07	0.07	−0.05	0.07
2.9	5541	12	163	11	0.01	0.06	−0.04	0.06
3.6	5502	12	145	6	−0.01	0.07	−0.12	0.07
4.8	5531	13	155	8	0.08	0.07	−0.10	0.07
7.0	5579	12	152	7	−0.04	0.06	−0.21	0.06
8.0	5573	39	179	23	0.14	0.19	−0.32	0.19
8.7	5575	18	95	22	−0.01	0.16	0.00	0.16
10.6	5596	48	138	82	0.14	0.30	0.09	0.30
12.0	5640	14	106	17	−0.00	0.11	0.01	0.11
13.7	5644	27	149	17	0.08	0.16	−0.10	0.16
15.5	5647	12	43	3	0.14	0.08	−0.06	0.08
17.2	5672	12	70	16	−0.00	0.09	0.19	0.09
19.5	5660	13	148	27	−0.26	0.08	0.15	0.08
22.6	5673	12	65	6	0.13	0.04	0.22	0.04
26.3	5680	12	42	12	−0.20	0.12	0.14	0.12
30.4	5693	12	38	2	0.08	0.09	−0.12	0.09
38.3	5696	12	47	2	0.15	0.07	−0.09	0.07

Table 6. Ionized-gas kinematics along the major axis of NGC 772.

r [″] (1)	V [km s^{-1}] (2)	δV (3)	σ [km s^{-1}] (4)	r [″] (5)	V [km s^{-1}] (6)	δV (7)	σ [km s^{-1}] (8)
−44.5	2600	12	0	0.3	2466	12	121
−29.2	2624	12	0	1.2	2446	12	96
−20.2	2682	12	72	2.1	2404	12	107
−17.2	2621	12	61	3.0	2348	12	54
−14.2	2610	12	46	3.9	2328	12	47
−11.7	2642	12	29	4.8	2361	12	65
−9.9	2615	12	33	5.7	2314	12	40
−8.4	2643	12	72	6.6	2344	12	65
−6.9	2624	12	44	8.6	2315	12	38
−6.0	2629	12	79	13.1	2303	12	41
−5.4	2614	12	53	16.0	2281	12	59
−3.9	2613	12	85	19.0	2267	12	39
−3.3	2604	12	64	22.0	2276	12	26
−2.4	2580	12	125	25.0	2284	12	55
−1.5	2557	12	135	34.0	2276	12	0
−0.6	2501	12	141	37.0	2275	12	33

ALICE, we fitted interactively a Gaussian to the emission line and a polynomial to its surrounding continuum. The central wavelength and FWHM (corrected for instrumental FWHM) of the fitting Gaussian were converted into radial velocity and velocity dispersion, respectively. The resulting velocities were corrected to the heliocentric frame of reference. At radii where the intensity of the relevant emission was low, we averaged from three to seven adjacent spectral rows to improve the signal-to-noise ratio of the line. The ionized-gas kinematics of NGC 772, 3898 and 7782 are described in Sections 5.1.1, 5.2.1 and 5.3.1, and the key parameters are tabulated in Tables 6–8. Each table provides the radial distance from the galaxy centre in arcsec, and the [O III] λ5006.8 (and the Hα only for NGC 3898) observed heliocentric velocity and velocity dispersion in km s^{-1}.

3.2 Broad-band imaging

The broad-band imaging of the three galaxies was carried out at the 1.83-m Vatican Advanced Technology Telescope (VATT) operated in the Mt. Graham International Observatory (Arizona,

Table 7. Ionized-gas kinematics along the major axis of NGC 3898.

r [″]	V [km s^{-1}]	δV	σ [km s^{-1}]	$\delta\sigma$	line[a]	r [″]	V [km s^{-1}]	δV	σ [km s^{-1}]	$\delta\sigma$	line[a]	r [″]	V [km s^{-1}]	δV	σ [km s^{-1}]	$\delta\sigma$	line[a]
(1)	(2)	(3)	(4)	(5)	(6)	(7)	(8)	(9)	(10)	(11)	(12)	(13)	(14)	(15)	(16)	(17)	(18)
−100.8	1411	1	5	5	2	−5.0	1298	9	88	9	2	6.6	1009	2	95	11	2
−98.8	1405	1	9	2	2	−4.7	1301	11	93	15	2	6.9	1010	2	83	13	2
−96.9	1410	1	9	0	2	−4.5	1296	12	97	0	1	7.2	1014	3	82	8	2
−94.4	1410	2	8	0	2	−4.3	1284	2	95	17	2	7.3	1025	12	96	0	1
−85.4	1389	6	13	0	2	−4.0	1278	2	101	15	2	7.6	1011	5	76	6	2
−79.5	1398	7	14	0	2	−3.9	1304	12	99	0	1	7.9	1008	4	84	9	2
−76.5	1389	4	6	0	2	−3.7	1280	1	68	1	2	8.2	985	12	97	0	1
−74.0	1390	4	26	0	2	−3.4	1276	6	81	10	2	8.2	993	3	83	6	2
−72.0	1389	3	16	1	2	−3.3	1252	12	114	0	1	8.6	985	1	70	9	2
−70.1	1389	1	12	2	2	−3.0	1270	3	79	22	2	9.2	988	2	69	5	2
−68.1	1387	1	13	1	2	−2.7	1262	6	93	24	2	9.4	963	12	88	0	1
−66.1	1390	1	11	0	2	−2.6	1190	12	109	0	1	10.2	985	1	62	10	2
−64.1	1388	4	20	3	2	−2.4	1238	15	94	34	2	10.9	971	12	88	0	1
−62.1	1385	2	25	2	2	−2.0	1222	16	98	38	2	11.2	977	7	64	7	2
−60.1	1379	1	28	5	2	−1.8	1185	12	74	0	1	12.2	963	5	54	0	2
−56.2	1379	1	27	0	2	−1.7	1199	10	107	25	2	12.4	961	12	63	0	1
−54.2	1372	2	20	2	2	−1.4	1196	3	94	21	2	13.2	947	4	44	2	2
−52.2	1385	2	22	6	2	−1.2	1179	12	88	0	1	13.9	941	12	41	0	1
−50.2	1388	2	21	1	2	−1.0	1194	3	90	20	2	14.2	953	2	48	1	2
−44.2	1384	4	41	0	2	−0.7	1191	2	96	18	2	15.2	958	1	41	4	2
−42.2	1361	3	38	0	2	−0.6	1162	12	160	0	1	16.2	944	12	75	0	1
−35.6	1377	1	0	0	2	−0.4	1188	1	96	15	2	16.7	963	1	29	3	2
−29.0	1380	11	24	1	2	−0.1	1179	4	105	11	2	18.7	968	2	30	0	2
−27.0	1363	1	44	0	2	−0.0	1160	12	129	0	1	19.2	952	12	45	0	1
−23.7	1359	3	35	13	2	0.3	1177	3	98	12	2	20.1	971	2	31	0	2
−21.1	1373	8	43	1	2	0.6	1177	12	100	0	1	20.6	952	4	13	13	2
−19.1	1384	1	44	8	2	0.6	1169	1	98	10	2	22.2	993	12	5	0	1
−17.1	1382	1	47	6	2	0.9	1159	3	96	18	2	22.6	955	2	35	0	2
−15.6	1401	10	35	1	2	1.2	1168	12	85	0	1	23.8	981	2	45	0	2
−14.6	1383	1	59	4	2	1.3	1152	2	92	11	2	25.3	989	4	43	10	2
−14.0	1385	12	101	0	1	1.6	1142	1	88	13	2	27.3	984	2	43	19	2
−13.6	1389	1	61	7	2	1.8	1144	12	79	0	1	29.2	984	3	35	5	2
−12.8	1398	12	112	0	1	1.9	1137	5	91	4	2	35.2	957	4	21	0	2
−12.6	1399	8	54	1	2	2.3	1131	5	78	8	2	39.2	948	1	28	3	2
−11.9	1421	12	96	0	1	2.4	1113	12	66	0	1	41.2	951	2	19	3	2
−11.6	1389	2	61	8	2	2.6	1123	4	84	9	2	43.2	945	3	16	3	2
−11.0	1399	12	91	0	1	2.9	1111	4	81	13	2	45.1	945	2	14	2	2
−10.6	1399	1	60	1	2	3.0	1074	12	82	0	1	47.1	947	2	18	0	2
−10.1	1427	12	95	0	1	3.3	1096	8	88	20	2	49.1	959	3	19	3	2
−9.6	1398	7	68	5	2	3.6	1087	12	82	0	1	51.1	962	1	21	4	2
−9.3	1412	12	23	0	1	3.6	1078	9	89	19	2	53.1	956	2	17	0	2
−8.7	1361	12	68	0	1	3.9	1057	6	87	19	2	55.1	954	1	14	2	2
−8.6	1379	12	75	2	2	4.2	1024	12	88	0	1	57.0	953	2	15	0	2
−8.1	1358	12	81	0	1	4.3	1041	11	88	14	2	59.0	958	1	11	0	2
−7.7	1336	1	57	8	2	4.6	1032	4	88	12	2	61.0	957	3	13	1	2
−7.5	1331	12	82	0	1	4.8	1038	12	77	0	1	63.0	946	3	9	2	2
−6.9	1327	12	67	0	1	4.9	1013	13	85	10	2	65.0	949	6	28	2	2
−6.7	1317	5	63	6	2	5.2	1006	10	85	13	2	67.0	950	1	15	0	2
−6.3	1327	12	89	0	1	5.4	1026	12	85	0	1	69.0	951	2	11	0	2
−6.0	1304	3	68	15	2	5.6	1000	12	93	6	2	70.9	954	1	7	4	2
−5.7	1317	12	76	0	1	5.9	1005	1	102	0	2	72.9	944	2	8	3	2
−5.7	1298	9	78	14	2	6.0	1002	12	85	0	1	74.9	942	1	16	1	2
−5.3	1300	1	73	11	2	6.2	1002	11	89	2	2	76.9	935	2	23	0	2
−5.1	1316	12	80	0	1	6.6	1027	12	72	0	1	88.8	939	2	15	0	2

[a] Observed emission line: 1 = [O III] λ5006.8 in MMT spectra, 2 = Hα in INT spectra.

Table 8. Ionized-gas kinematics along the major axis of NGC 7782.

r [″] (1)	V [km s^{-1}] (2)	δV (3)	σ [km s^{-1}] (4)	r [″] (5)	V [km s^{-1}] (6)	δV (7)	σ [km s^{-1}] (8)
−27.1	5132	12	42	1.4	5579	12	102
−24.1	5206	12	78	2.0	5573	12	111
−21.1	5184	12	69	2.8	5564	12	83
−18.1	5154	12	53	4.1	5641	12	31
−15.1	5181	12	0	6.4	5652	12	0
−9.1	5209	12	0	8.9	5641	12	34
−6.9	5203	12	66	11.9	5689	12	58
−5.4	5193	12	98	17.5	5630	12	81
−3.9	5190	12	79	28.6	5714	12	65
−2.8	5192	12	47	33.5	5653	12	49
−2.2	5230	12	78	35.1	5697	12	0
−1.6	5203	12	103	36.9	5690	12	32
−1.0	5226	12	118	38.0	5653	12	125
−0.4	5315	12	138	39.0	5690	12	20
0.2	5439	12	179	43.0	5699	12	24
0.8	5519	12	172				

USA) in two observing runs in 1997 March and November. A back-illuminated 2048×2048 Loral CCD with $15 \times 15\,\mu m^2$ pixels was used as detector at the aplanatic Gregorian focus ($f/9$) of the telescope. It yielded a field of view of $6.4 \times 6.4\,arcmin^2$, with an image scale of $0.4\,arcsec\,pixel^{-1}$ after a 2×2 pixel binning. The gain and the readout noise were $1.4\,e^-\,ADU^{-1}$ and $6.5\,e^-$, respectively.

At regular intervals during each night, different bias frames (typically 10) were taken to check possible slight bias-level variations. All galaxies were observed twice in the Johnson V band. The date and the duration of all the exposures are given in Table 9. A number of twilight sky flats were taken at the beginning and at the end of the nights. No photometric standard was observed.

The data reduction was carried out using standard IRAF[2] routines. All the frames were bias-subtracted and corrected for pixel-to-pixel intensity variations by using a mean flat-field for each night. The different frames of each galaxy were shifted and aligned to an accuracy of a few hundredths of a pixel using common field stars as reference. After checking that their point spread functions (PSFs) were comparable, the frames were averaged to obtain a single V-band image. The cosmic rays were identified and removed during the averaging routine. Two-dimensional Gaussian fits to the field stars in the resulting images yielded the final FWHM measurement of seeing PSF listed in Table 3. In each final frame the mean value of the sky level was determined in a large number of 5×5 pixel areas. These areas were selected in empty regions of the frames, which were free of objects and far from the galaxy to avoid the contamination of the light of field stars and galaxies, as well as of the target galaxy itself. The sky value of each frame is the average of these mean values. For the estimate of error in the sky determination we adopted half the difference between the maximum and minimum of the mean values obtained for the small areas.

For each galaxy we derived a 'luminosity growth curve' by measuring the integrated magnitudes within circular apertures of increasing radius by means of the IRAF task ELLIPSE within the STSDAS package. Absolute calibration was performed by fitting the constant portion of the growth curves (Fig. 1) to the corresponding total magnitude V_T given by RC3.

Before fitting ellipses to the galaxy images, we removed the field stars using the IRAF routines within the DAOPHOT package. Special care was taken to remove saturated stars and field galaxies, which were edited out by hand, and removed by replacing them with the local average of counts. When bright stars were too close to the galaxy, their light was masked out to where the galaxy light started to be dominant. For each galaxy we derived the surface-brightness profile and isophotal shape parameters by ellipse-fitting to its isophotes using the isophote-fitting program ELLIPSE (see Jedrzejewky 1987 for details on the fitting procedure). The resulting surface brightness, ellipticity, position angle and $\cos 4\theta$ Fourier coefficient radial profiles for NGC 772, 3898 and 7782 are presented in Sections 5.1.2, 5.2.2 and 5.3.2, and tabulated in Tables 10, 11 and 12. Each table provides the isophotal semimajor axis in arcsec, surface brightness in mag arcsec^{-2}, ellipticity, position angle in degrees, and the $\cos 4\theta$ Fourier coefficient.

[2] IRAF is distributed by the National Optical Astronomy Observatories which are operated by the Association of Universities for Research in Astronomy (AURA) under cooperative agreement with the National Science Foundation.

Table 9. Log of the broad and narrow-band observations.

Object	Date	Filter	t_{exp} [s]	Seeing[a] [″]
NGC 772	02 Nov 1997	V	2×180	1.7
	07 Nov 1997	r6450	4×600	1.9
	07 Nov 1997	r6630	4×600	1.8
NGC 3898	11 Mar 1997	V	2×60	1.4
	11 Mar 1997	r6450	$4 \times 540,\ 2 \times 600$	1.3
	11 Mar 1997	r6580	$2 \times 500,\ 2 \times 540$	1.3
NGC 7782	02 Nov 1997	V	2×360	2.2
	10 Nov 1997	r6450	3×600	1.8
	10 Nov 1997	r6680	3×600	2.2

[a] Seeing FWHM measured on the final resulting frame.

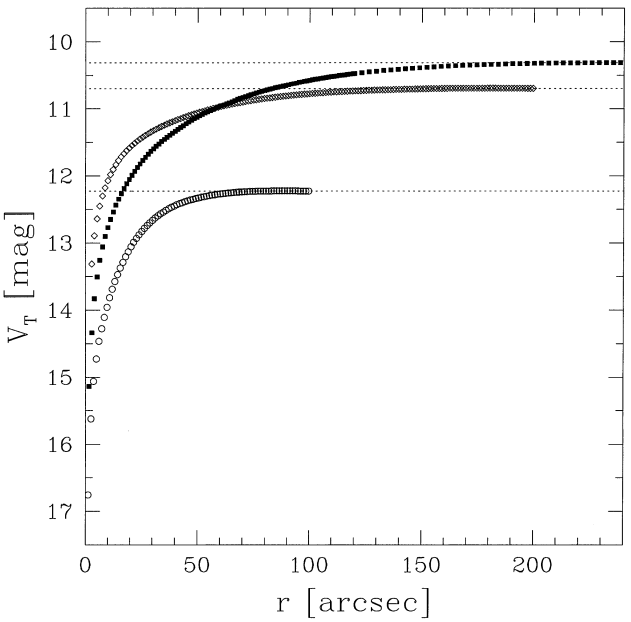

Figure 1. Calibrated luminosity growth curves of NGC 772 (*filled squares*, $V_T = 10.31$ mag), NGC 3898 (*open diamonds*, $V_T = 10.70$ mag) and NGC 7782 (*open circles*, $V_T = 12.23$ mag). For each galaxy the *dotted line* shows the asymptotic magnitude taken from RC3.

Table 10. Surface photometry of NGC 772.

r [″] (1)	μ_V [mag arcsec^{-2}] (2)	ϵ (3)	PA [°] (4)	$\cos 4\theta$ (5)	r [″] (6)	μ_V [mag arcsec^{-2}] (7)	ϵ (8)	PA [°] (9)	$\cos 4\theta$ (10)
1.6	17.77 ± 0.04	0.08 ± 0.01	127.1 ± 3.7	0.005 ± 0.001	82.0	22.22 ± 0.03	0.36 ± 0.01	130.8 ± 1.1	0.038 ± 0.009
2.8	18.26 ± 0.02	0.15 ± 0.01	116.4 ± 1.2	0.015 ± 0.001	83.2	22.25 ± 0.03	0.36 ± 0.01	129.9 ± 1.3	0.037 ± 0.011
4.0	18.59 ± 0.01	0.18 ± 0.01	116.2 ± 0.6	0.005 ± 0.001	84.4	22.26 ± 0.03	0.37 ± 0.01	130.2 ± 1.3	0.042 ± 0.012
5.2	18.86 ± 0.01	0.18 ± 0.01	119.5 ± 0.6	0.002 ± 0.002	85.6	22.28 ± 0.03	0.37 ± 0.01	128.6 ± 1.2	0.026 ± 0.012
6.4	19.09 ± 0.01	0.19 ± 0.01	122.0 ± 0.5	0.004 ± 0.002	86.8	22.32 ± 0.02	0.37 ± 0.01	128.6 ± 1.2	0.022 ± 0.013
7.6	19.31 ± 0.01	0.21 ± 0.01	122.7 ± 0.4	0.003 ± 0.001	88.0	22.33 ± 0.02	0.37 ± 0.02	127.1 ± 1.5	0.007 ± 0.024
8.8	19.49 ± 0.02	0.24 ± 0.01	125.1 ± 0.5	0.006 ± 0.002	89.2	22.33 ± 0.03	0.37 ± 0.01	123.2 ± 1.0	−0.023 ± 0.008
10.0	19.61 ± 0.02	0.29 ± 0.01	127.0 ± 0.7	0.013 ± 0.004	90.4	22.35 ± 0.03	0.37 ± 0.02	121.5 ± 1.5	−0.062 ± 0.031
11.2	19.71 ± 0.02	0.33 ± 0.01	125.6 ± 0.5	0.020 ± 0.003	91.6	22.35 ± 0.03	0.37 ± 0.01	120.1 ± 1.1	−0.050 ± 0.013
12.4	19.81 ± 0.02	0.37 ± 0.01	122.4 ± 0.3	0.011 ± 0.003	92.8	22.36 ± 0.03	0.37 ± 0.01	120.1 ± 1.0	−0.041 ± 0.011
13.6	19.89 ± 0.03	0.39 ± 0.01	117.4 ± 0.6	−0.013 ± 0.005	94.0	22.33 ± 0.06	0.37 ± 0.02	112.4 ± 1.7	−0.101 ± 0.015
14.8	19.97 ± 0.03	0.39 ± 0.01	110.6 ± 0.8	−0.032 ± 0.007	95.2	22.36 ± 0.05	0.37 ± 0.02	114.4 ± 1.6	−0.075 ± 0.015
16.0	20.18 ± 0.03	0.26 ± 0.01	106.6 ± 1.2	0.029 ± 0.006	96.4	22.40 ± 0.03	0.37 ± 0.01	114.4 ± 0.7	−0.037 ± 0.006
17.2	20.27 ± 0.02	0.24 ± 0.01	116.3 ± 1.2	−0.016 ± 0.004	97.6	22.45 ± 0.03	0.37 ± 0.01	114.4 ± 0.6	−0.027 ± 0.006
18.4	20.36 ± 0.02	0.24 ± 0.01	123.4 ± 1.6	−0.035 ± 0.007	98.8	22.49 ± 0.03	0.37 ± 0.01	116.8 ± 0.6	−0.015 ± 0.006
19.6	20.42 ± 0.02	0.26 ± 0.01	128.4 ± 1.9	−0.040 ± 0.011	100.0	22.50 ± 0.03	0.38 ± 0.01	116.1 ± 0.6	−0.026 ± 0.006
20.8	20.47 ± 0.03	0.29 ± 0.02	129.6 ± 2.0	−0.023 ± 0.013	101.2	22.52 ± 0.03	0.38 ± 0.01	118.4 ± 0.7	−0.023 ± 0.007
22.0	20.51 ± 0.02	0.30 ± 0.01	125.7 ± 1.6	−0.026 ± 0.010	102.4	22.55 ± 0.03	0.37 ± 0.01	121.4 ± 0.9	−0.011 ± 0.007
23.2	20.57 ± 0.02	0.29 ± 0.01	120.6 ± 1.4	−0.011 ± 0.009	103.6	22.60 ± 0.03	0.37 ± 0.01	121.4 ± 1.1	−0.008 ± 0.012
24.4	20.65 ± 0.02	0.29 ± 0.01	119.9 ± 1.5	0.004 ± 0.013	104.8	22.63 ± 0.03	0.37 ± 0.01	121.4 ± 1.1	−0.005 ± 0.012
25.6	20.68 ± 0.02	0.30 ± 0.01	115.3 ± 1.0	−0.023 ± 0.006	106.0	22.67 ± 0.03	0.37 ± 0.01	121.4 ± 1.3	0.002 ± 0.013
26.8	20.84 ± 0.02	0.15 ± 0.02	110.3 ± 3.6	−0.016 ± 0.014	107.2	22.69 ± 0.03	0.37 ± 0.01	121.4 ± 1.2	0.010 ± 0.012
28.0	20.85 ± 0.03	0.18 ± 0.02	97.5 ± 3.4	−0.034 ± 0.011	108.4	22.81 ± 0.04	0.31 ± 0.02	126.4 ± 1.7	0.046 ± 0.009
29.2	20.91 ± 0.03	0.17 ± 0.02	102.1 ± 3.3	−0.037 ± 0.010	109.6	22.71 ± 0.04	0.37 ± 0.01	122.0 ± 1.1	0.019 ± 0.008
30.4	20.94 ± 0.03	0.19 ± 0.01	107.5 ± 2.2	−0.029 ± 0.007	110.8	22.77 ± 0.04	0.34 ± 0.01	125.4 ± 1.4	0.044 ± 0.008
31.6	21.00 ± 0.02	0.19 ± 0.01	111.7 ± 1.7	−0.018 ± 0.006	112.0	22.74 ± 0.04	0.35 ± 0.01	125.7 ± 1.4	0.057 ± 0.009
32.8	21.07 ± 0.02	0.20 ± 0.01	115.7 ± 1.5	−0.019 ± 0.005	113.2	22.76 ± 0.05	0.35 ± 0.02	125.7 ± 1.6	0.065 ± 0.011
34.0	21.13 ± 0.02	0.20 ± 0.01	116.5 ± 1.3	−0.023 ± 0.005	114.4	22.81 ± 0.05	0.35 ± 0.02	125.7 ± 1.6	0.066 ± 0.011
35.2	21.14 ± 0.02	0.23 ± 0.01	122.1 ± 1.1	−0.028 ± 0.005	115.6	22.86 ± 0.04	0.36 ± 0.01	126.9 ± 1.4	0.058 ± 0.009
36.4	21.18 ± 0.02	0.25 ± 0.01	122.1 ± 1.0	−0.027 ± 0.004	116.8	22.88 ± 0.04	0.36 ± 0.01	125.0 ± 1.2	0.059 ± 0.008
37.6	21.22 ± 0.02	0.27 ± 0.01	122.1 ± 0.9	−0.030 ± 0.004	118.0	22.88 ± 0.04	0.35 ± 0.01	122.3 ± 1.0	0.038 ± 0.006
38.8	21.27 ± 0.02	0.27 ± 0.01	122.2 ± 1.0	−0.037 ± 0.005	119.2	22.91 ± 0.03	0.37 ± 0.01	123.8 ± 1.0	0.044 ± 0.006
40.0	21.30 ± 0.02	0.29 ± 0.01	123.1 ± 1.1	−0.038 ± 0.006	120.0	22.93 ± 0.04	0.36 ± 0.01	121.7 ± 0.9	0.027 ± 0.005
41.2	21.36 ± 0.02	0.29 ± 0.01	123.7 ± 1.5	−0.047 ± 0.010	123.2	22.96 ± 0.04	0.37 ± 0.01	123.0 ± 0.8	0.021 ± 0.005
42.4	21.40 ± 0.02	0.29 ± 0.02	123.7 ± 1.9	−0.044 ± 0.015	126.4	23.12 ± 0.04	0.32 ± 0.01	124.9 ± 0.5	0.010 ± 0.003
43.6	21.39 ± 0.02	0.33 ± 0.01	123.7 ± 1.2	−0.022 ± 0.010	129.6	23.18 ± 0.04	0.32 ± 0.01	125.3 ± 0.6	0.013 ± 0.003
44.8	21.42 ± 0.02	0.33 ± 0.01	122.9 ± 1.2	−0.001 ± 0.009	132.8	23.25 ± 0.04	0.33 ± 0.01	125.9 ± 0.5	0.009 ± 0.003
46.0	21.42 ± 0.02	0.35 ± 0.01	122.9 ± 0.9	−0.000 ± 0.007	136.0	23.35 ± 0.04	0.33 ± 0.01	127.2 ± 0.5	0.004 ± 0.003
47.2	21.45 ± 0.02	0.36 ± 0.01	122.5 ± 0.9	0.004 ± 0.007	139.2	23.39 ± 0.05	0.35 ± 0.01	127.2 ± 0.5	0.003 ± 0.003
48.4	21.48 ± 0.02	0.31 ± 0.01	117.0 ± 0.6	−0.003 ± 0.004	142.4	23.47 ± 0.05	0.35 ± 0.01	128.9 ± 0.5	0.006 ± 0.003
49.6	21.62 ± 0.02	0.16 ± 0.01	127.6 ± 1.8	0.024 ± 0.005	145.6	23.52 ± 0.05	0.36 ± 0.01	128.7 ± 0.5	0.006 ± 0.003
50.8	21.68 ± 0.03	0.15 ± 0.01	132.5 ± 2.3	0.006 ± 0.006	148.8	23.57 ± 0.05	0.37 ± 0.01	128.7 ± 0.5	0.011 ± 0.003
52.0	21.71 ± 0.02	0.15 ± 0.01	138.0 ± 1.7	−0.028 ± 0.004	152.0	23.67 ± 0.06	0.37 ± 0.01	128.2 ± 0.5	0.018 ± 0.004
53.2	21.72 ± 0.02	0.17 ± 0.01	138.0 ± 1.6	−0.028 ± 0.005	155.2	23.75 ± 0.06	0.37 ± 0.01	127.0 ± 0.5	0.011 ± 0.003
54.4	21.74 ± 0.02	0.19 ± 0.01	140.8 ± 1.4	−0.032 ± 0.004	158.4	23.79 ± 0.06	0.37 ± 0.01	126.2 ± 0.4	0.010 ± 0.003
55.6	21.75 ± 0.02	0.21 ± 0.01	141.3 ± 1.2	−0.023 ± 0.004	161.6	23.81 ± 0.06	0.38 ± 0.01	125.1 ± 0.4	0.006 ± 0.003
56.8	21.79 ± 0.02	0.21 ± 0.01	140.7 ± 1.4	−0.001 ± 0.005	164.8	23.80 ± 0.06	0.40 ± 0.01	124.3 ± 0.4	0.008 ± 0.003
58.0	21.79 ± 0.02	0.24 ± 0.02	140.7 ± 2.4	−0.009 ± 0.019	168.0	23.89 ± 0.07	0.40 ± 0.01	123.6 ± 0.4	0.001 ± 0.004
59.2	21.83 ± 0.02	0.24 ± 0.02	142.9 ± 2.8	0.042 ± 0.063	171.2	23.99 ± 0.07	0.40 ± 0.01	122.5 ± 0.4	0.000 ± 0.003
60.4	21.84 ± 0.02	0.26 ± 0.01	142.9 ± 1.5	0.028 ± 0.019	174.4	24.18 ± 0.08	0.39 ± 0.01	122.5 ± 0.6	0.034 ± 0.005
61.6	21.83 ± 0.02	0.28 ± 0.01	139.6 ± 1.0	0.009 ± 0.006	177.6	24.28 ± 0.09	0.38 ± 0.01	121.0 ± 0.7	0.031 ± 0.005
62.8	21.87 ± 0.02	0.28 ± 0.01	139.6 ± 1.1	0.008 ± 0.009	180.8	24.23 ± 0.09	0.41 ± 0.01	120.1 ± 0.9	0.027 ± 0.007
64.0	21.93 ± 0.04	0.22 ± 0.02	132.3 ± 2.7	0.001 ± 0.013	184.0	24.30 ± 0.10	0.35 ± 0.01	113.6 ± 1.3	0.053 ± 0.010
65.2	21.87 ± 0.03	0.30 ± 0.02	136.5 ± 1.8	−0.033 ± 0.012	187.2	24.29 ± 0.09	0.41 ± 0.01	116.6 ± 0.6	0.005 ± 0.005
66.4	21.91 ± 0.03	0.30 ± 0.01	134.9 ± 1.2	−0.030 ± 0.007	190.4	24.33 ± 0.10	0.41 ± 0.01	117.3 ± 0.9	0.032 ± 0.009
67.6	21.97 ± 0.02	0.30 ± 0.01	134.9 ± 0.8	−0.002 ± 0.005	193.6	24.31 ± 0.09	0.41 ± 0.01	113.1 ± 0.8	−0.028 ± 0.010
68.8	22.00 ± 0.02	0.30 ± 0.01	137.8 ± 0.7	0.024 ± 0.004	196.8	24.37 ± 0.10	0.41 ± 0.01	113.1 ± 0.6	−0.020 ± 0.007
70.0	22.01 ± 0.04	0.28 ± 0.01	135.0 ± 1.8	0.021 ± 0.011	200.0	24.60 ± 0.12	0.34 ± 0.01	109.4 ± 0.8	0.033 ± 0.006
71.2	22.05 ± 0.03	0.29 ± 0.01	135.0 ± 1.3	0.027 ± 0.008	203.2	24.70 ± 0.13	0.34 ± 0.01	109.0 ± 1.0	0.044 ± 0.008
72.4	22.07 ± 0.02	0.30 ± 0.01	135.0 ± 1.1	0.038 ± 0.008	206.4	24.73 ± 0.14	0.35 ± 0.01	108.1 ± 0.7	0.028 ± 0.005
73.6	22.13 ± 0.02	0.30 ± 0.01	135.0 ± 0.9	0.053 ± 0.008	209.6	24.79 ± 0.15	0.35 ± 0.01	108.1 ± 0.9	0.048 ± 0.007
74.8	22.17 ± 0.02	0.30 ± 0.01	135.0 ± 0.9	0.061 ± 0.006	212.8	24.87 ± 0.16	0.35 ± 0.01	106.8 ± 0.8	0.023 ± 0.008
76.0	22.20 ± 0.02	0.30 ± 0.01	135.0 ± 0.9	0.063 ± 0.005	216.0	24.80 ± 0.15	0.37 ± 0.01	109.5 ± 0.9	0.047 ± 0.008
77.2	22.21 ± 0.02	0.31 ± 0.01	134.2 ± 0.8	0.059 ± 0.005	219.2	24.92 ± 0.16	0.37 ± 0.01	109.5 ± 1.1	0.055 ± 0.010
78.4	22.19 ± 0.02	0.32 ± 0.01	129.5 ± 0.7	0.022 ± 0.005	222.4	25.00 ± 0.18	0.36 ± 0.01	108.2 ± 1.3	0.061 ± 0.014
79.6	22.19 ± 0.02	0.34 ± 0.01	130.9 ± 0.7	0.032 ± 0.005	225.6	25.17 ± 0.21	0.33 ± 0.02	109.2 ± 2.2	0.093 ± 0.017
80.8	22.20 ± 0.02	0.35 ± 0.01	130.9 ± 0.8	0.037 ± 0.006	228.8	25.10 ± 0.19	0.36 ± 0.02	109.7 ± 2.2	0.095 ± 0.022

Table 11. Surface photometry of NGC 3898.

r [″] (1)	μ_V [mag arcsec^{-2}] (2)	ϵ (3)	PA [°] (4)	$\cos 4\theta$ (5)	r [″] (6)	μ_V [mag arcsec^{-2}] (7)	ϵ (8)	PA [°] (9)	$\cos 4\theta$ (10)
2.8	17.25 ± 0.01	0.23 ± 0.01	108.2 ± 0.3	0.003 ± 0.001	84.4	22.93 ± 0.01	0.45 ± 0.02	108.9 ± 0.4	0.011 ± 0.004
4.0	17.71 ± 0.01	0.26 ± 0.01	108.6 ± 0.2	0.001 ± 0.001	85.6	22.97 ± 0.02	0.45 ± 0.02	108.9 ± 0.4	0.011 ± 0.004
5.2	18.10 ± 0.01	0.27 ± 0.01	109.8 ± 0.2	−0.001 ± 0.001	86.8	23.03 ± 0.02	0.44 ± 0.01	108.7 ± 0.4	0.009 ± 0.004
6.4	18.42 ± 0.02	0.29 ± 0.01	110.8 ± 0.4	−0.006 ± 0.002	88.0	23.03 ± 0.02	0.44 ± 0.01	108.7 ± 0.4	0.009 ± 0.004
7.6	18.65 ± 0.02	0.31 ± 0.02	109.8 ± 0.4	−0.007 ± 0.002	89.2	23.04 ± 0.02	0.45 ± 0.02	108.7 ± 0.4	0.005 ± 0.004
8.8	18.84 ± 0.01	0.33 ± 0.01	109.0 ± 0.3	−0.002 ± 0.002	90.4	23.08 ± 0.02	0.45 ± 0.01	107.7 ± 0.4	0.006 ± 0.004
10.0	19.00 ± 0.01	0.35 ± 0.01	108.4 ± 0.3	0.005 ± 0.002	91.6	23.13 ± 0.02	0.44 ± 0.01	108.4 ± 0.3	0.007 ± 0.004
11.2	19.15 ± 0.01	0.37 ± 0.01	108.2 ± 0.2	0.008 ± 0.001	92.8	23.18 ± 0.02	0.44 ± 0.01	108.3 ± 0.4	0.008 ± 0.004
12.4	19.29 ± 0.01	0.39 ± 0.01	108.2 ± 0.2	0.009 ± 0.001	94.0	23.21 ± 0.02	0.44 ± 0.01	109.0 ± 0.5	0.024 ± 0.005
13.6	19.44 ± 0.01	0.39 ± 0.01	108.1 ± 0.2	0.005 ± 0.001	95.2	23.25 ± 0.02	0.44 ± 0.01	109.5 ± 0.4	0.017 ± 0.004
14.8	19.59 ± 0.01	0.39 ± 0.01	108.5 ± 0.2	0.008 ± 0.001	96.4	23.32 ± 0.02	0.44 ± 0.01	108.8 ± 0.4	0.015 ± 0.005
16.0	19.73 ± 0.01	0.39 ± 0.02	108.9 ± 0.2	0.011 ± 0.001	97.6	23.39 ± 0.02	0.42 ± 0.01	108.3 ± 0.4	0.010 ± 0.004
17.2	19.86 ± 0.01	0.39 ± 0.02	109.0 ± 0.2	0.010 ± 0.001	98.8	23.39 ± 0.02	0.43 ± 0.02	109.2 ± 0.4	0.001 ± 0.004
18.4	20.01 ± 0.01	0.39 ± 0.01	108.8 ± 0.2	0.003 ± 0.001	100.0	23.46 ± 0.02	0.42 ± 0.01	109.2 ± 0.5	0.005 ± 0.004
19.6	20.14 ± 0.01	0.39 ± 0.01	108.5 ± 0.1	−0.001 ± 0.001	101.2	23.55 ± 0.02	0.41 ± 0.01	109.3 ± 0.5	0.015 ± 0.005
20.8	20.25 ± 0.01	0.39 ± 0.01	108.4 ± 0.2	−0.002 ± 0.001	102.4	23.56 ± 0.02	0.41 ± 0.01	109.2 ± 0.5	0.014 ± 0.005
22.0	20.37 ± 0.01	0.39 ± 0.01	108.6 ± 0.2	−0.001 ± 0.001	103.6	23.63 ± 0.02	0.41 ± 0.01	109.0 ± 0.6	0.028 ± 0.005
23.2	20.47 ± 0.01	0.40 ± 0.02	109.1 ± 0.2	−0.003 ± 0.001	104.8	23.66 ± 0.02	0.40 ± 0.01	109.7 ± 0.6	0.029 ± 0.006
24.4	20.55 ± 0.01	0.40 ± 0.01	109.1 ± 0.2	−0.003 ± 0.002	106.0	23.71 ± 0.02	0.39 ± 0.01	108.4 ± 0.6	0.014 ± 0.005
25.6	20.63 ± 0.01	0.41 ± 0.01	109.0 ± 0.2	0.003 ± 0.002	107.2	23.79 ± 0.03	0.38 ± 0.01	108.0 ± 0.6	0.024 ± 0.006
26.8	20.71 ± 0.01	0.42 ± 0.01	108.3 ± 0.2	0.004 ± 0.002	108.4	23.84 ± 0.03	0.37 ± 0.01	108.0 ± 0.6	0.013 ± 0.005
28.0	20.82 ± 0.01	0.41 ± 0.01	107.6 ± 0.2	0.014 ± 0.002	109.6	23.86 ± 0.03	0.38 ± 0.01	108.0 ± 0.6	0.005 ± 0.005
29.2	20.91 ± 0.01	0.39 ± 0.01	108.1 ± 0.3	0.019 ± 0.002	110.8	23.90 ± 0.03	0.38 ± 0.01	108.3 ± 0.7	0.009 ± 0.006
30.4	20.99 ± 0.01	0.39 ± 0.01	107.8 ± 0.3	0.018 ± 0.002	112.0	23.92 ± 0.03	0.38 ± 0.01	107.0 ± 0.7	0.011 ± 0.006
31.6	21.05 ± 0.01	0.40 ± 0.01	106.9 ± 0.3	0.013 ± 0.003	113.2	23.96 ± 0.03	0.38 ± 0.01	108.3 ± 0.7	−0.000 ± 0.006
32.8	21.12 ± 0.01	0.40 ± 0.02	107.5 ± 0.3	0.018 ± 0.003	114.4	23.99 ± 0.03	0.38 ± 0.01	106.9 ± 0.7	0.004 ± 0.007
34.0	21.21 ± 0.01	0.39 ± 0.02	107.9 ± 0.3	0.020 ± 0.002	115.6	24.07 ± 0.03	0.37 ± 0.01	108.0 ± 0.9	−0.017 ± 0.007
35.2	21.27 ± 0.01	0.38 ± 0.02	108.0 ± 0.3	0.008 ± 0.002	116.8	24.15 ± 0.04	0.36 ± 0.01	108.0 ± 0.9	0.019 ± 0.007
36.4	21.33 ± 0.01	0.38 ± 0.02	108.8 ± 0.3	0.001 ± 0.003	118.0	24.17 ± 0.04	0.35 ± 0.01	107.6 ± 0.9	0.027 ± 0.007
37.6	21.38 ± 0.01	0.38 ± 0.01	109.1 ± 0.3	−0.007 ± 0.003	119.2	24.20 ± 0.04	0.36 ± 0.01	110.4 ± 1.1	0.016 ± 0.009
38.8	21.42 ± 0.01	0.39 ± 0.02	109.3 ± 0.3	−0.010 ± 0.003	120.4	24.17 ± 0.04	0.37 ± 0.01	108.6 ± 0.8	0.014 ± 0.007
40.0	21.47 ± 0.02	0.40 ± 0.02	109.5 ± 0.3	−0.003 ± 0.003	121.6	24.20 ± 0.04	0.37 ± 0.01	111.4 ± 0.7	0.016 ± 0.006
41.2	21.50 ± 0.02	0.40 ± 0.02	109.2 ± 0.3	−0.006 ± 0.003	122.8	24.27 ± 0.04	0.36 ± 0.01	109.7 ± 0.8	−0.000 ± 0.006
42.4	21.54 ± 0.01	0.41 ± 0.02	108.5 ± 0.3	−0.014 ± 0.003	124.0	24.29 ± 0.04	0.36 ± 0.01	108.8 ± 0.8	−0.005 ± 0.007
43.6	21.57 ± 0.01	0.42 ± 0.02	108.5 ± 0.3	−0.010 ± 0.003	125.2	24.38 ± 0.04	0.36 ± 0.01	109.9 ± 0.8	0.007 ± 0.007
44.8	21.58 ± 0.01	0.43 ± 0.02	108.0 ± 0.3	−0.001 ± 0.003	126.4	24.37 ± 0.04	0.37 ± 0.01	108.9 ± 1.1	0.028 ± 0.009
46.0	21.61 ± 0.01	0.44 ± 0.02	107.9 ± 0.3	0.001 ± 0.003	127.6	24.29 ± 0.04	0.39 ± 0.01	110.1 ± 0.8	0.018 ± 0.007
47.2	21.62 ± 0.01	0.45 ± 0.02	108.1 ± 0.3	0.008 ± 0.003	128.8	24.50 ± 0.05	0.36 ± 0.01	109.4 ± 1.0	0.022 ± 0.009
48.4	21.67 ± 0.01	0.45 ± 0.02	107.6 ± 0.3	0.002 ± 0.003	130.0	24.47 ± 0.04	0.37 ± 0.01	109.8 ± 0.9	0.019 ± 0.008
49.6	21.69 ± 0.01	0.46 ± 0.02	107.6 ± 0.3	0.007 ± 0.003	131.2	24.49 ± 0.04	0.37 ± 0.01	111.2 ± 0.7	0.005 ± 0.006
50.8	21.71 ± 0.01	0.47 ± 0.01	108.1 ± 0.3	0.010 ± 0.003	132.4	24.59 ± 0.05	0.36 ± 0.01	111.2 ± 1.0	−0.010 ± 0.009
52.0	21.75 ± 0.01	0.48 ± 0.02	108.1 ± 0.3	0.022 ± 0.003	133.6	24.65 ± 0.05	0.35 ± 0.01	111.2 ± 1.1	−0.012 ± 0.010
53.2	21.79 ± 0.01	0.48 ± 0.02	107.7 ± 0.2	0.015 ± 0.003	134.8	24.69 ± 0.05	0.37 ± 0.01	109.2 ± 1.3	−0.015 ± 0.011
54.4	21.81 ± 0.01	0.49 ± 0.02	108.0 ± 0.2	0.019 ± 0.003	136.0	24.73 ± 0.05	0.36 ± 0.01	111.9 ± 1.3	−0.006 ± 0.013
55.6	21.84 ± 0.01	0.49 ± 0.02	107.9 ± 0.3	0.024 ± 0.003	137.2	24.76 ± 0.05	0.36 ± 0.01	109.1 ± 1.2	0.005 ± 0.010
56.8	21.88 ± 0.01	0.49 ± 0.02	108.2 ± 0.2	0.029 ± 0.003	138.4	24.81 ± 0.06	0.36 ± 0.01	109.6 ± 1.2	−0.013 ± 0.011
58.0	21.93 ± 0.01	0.49 ± 0.02	108.3 ± 0.2	0.022 ± 0.003	139.6	24.80 ± 0.06	0.38 ± 0.02	111.4 ± 1.7	−0.049 ± 0.021
59.2	21.98 ± 0.01	0.49 ± 0.01	107.7 ± 0.3	0.015 ± 0.003	140.8	24.74 ± 0.05	0.38 ± 0.01	113.0 ± 1.3	−0.007 ± 0.015
60.4	22.02 ± 0.01	0.49 ± 0.01	107.9 ± 0.3	0.019 ± 0.003	142.0	24.83 ± 0.06	0.37 ± 0.02	108.4 ± 1.8	0.005 ± 0.016
61.6	22.06 ± 0.01	0.49 ± 0.02	108.1 ± 0.3	0.015 ± 0.004	143.2	24.78 ± 0.05	0.39 ± 0.01	110.9 ± 1.0	0.013 ± 0.009
62.8	22.11 ± 0.01	0.49 ± 0.01	108.1 ± 0.3	0.019 ± 0.003	144.4	24.84 ± 0.06	0.39 ± 0.01	110.8 ± 1.0	−0.013 ± 0.010
64.0	22.22 ± 0.02	0.45 ± 0.01	109.4 ± 0.5	0.050 ± 0.005	145.6	24.89 ± 0.06	0.37 ± 0.01	108.9 ± 1.1	0.016 ± 0.010
65.2	22.27 ± 0.01	0.45 ± 0.02	109.4 ± 0.3	0.034 ± 0.003	146.8	24.96 ± 0.06	0.38 ± 0.01	107.8 ± 0.9	0.006 ± 0.008
66.4	22.32 ± 0.01	0.45 ± 0.02	109.4 ± 0.3	0.032 ± 0.004	148.0	25.08 ± 0.07	0.36 ± 0.01	109.7 ± 1.2	0.017 ± 0.012
67.6	22.28 ± 0.01	0.48 ± 0.02	108.6 ± 0.4	0.032 ± 0.004	149.2	25.04 ± 0.07	0.36 ± 0.01	108.1 ± 1.3	0.014 ± 0.012
68.8	22.33 ± 0.01	0.48 ± 0.02	108.8 ± 0.3	0.028 ± 0.003	150.4	25.17 ± 0.08	0.37 ± 0.01	107.7 ± 1.3	0.014 ± 0.011
70.0	22.35 ± 0.01	0.48 ± 0.02	108.8 ± 0.3	0.032 ± 0.004	151.6	25.09 ± 0.07	0.38 ± 0.01	110.4 ± 1.2	−0.018 ± 0.011
71.2	22.39 ± 0.01	0.48 ± 0.02	108.3 ± 0.3	0.034 ± 0.004	152.8	25.19 ± 0.08	0.38 ± 0.01	109.8 ± 1.1	0.001 ± 0.010
72.4	22.40 ± 0.01	0.49 ± 0.02	107.9 ± 0.3	0.037 ± 0.004	154.0	25.11 ± 0.08	0.38 ± 0.01	109.1 ± 1.4	0.010 ± 0.013
73.6	22.43 ± 0.01	0.49 ± 0.02	107.3 ± 0.3	0.029 ± 0.003	155.2	25.12 ± 0.07	0.40 ± 0.01	109.2 ± 1.0	−0.013 ± 0.010
74.8	22.45 ± 0.01	0.50 ± 0.02	107.7 ± 0.2	0.028 ± 0.003	156.4	25.15 ± 0.08	0.39 ± 0.01	110.4 ± 1.2	0.030 ± 0.011
76.0	22.50 ± 0.02	0.50 ± 0.02	107.8 ± 0.3	0.036 ± 0.003	157.6	25.10 ± 0.08	0.41 ± 0.01	110.1 ± 1.0	0.024 ± 0.010
77.2	22.55 ± 0.01	0.49 ± 0.02	107.7 ± 0.2	0.025 ± 0.003	158.8	25.31 ± 0.09	0.38 ± 0.02	111.2 ± 1.4	0.038 ± 0.013
78.4	22.62 ± 0.01	0.48 ± 0.02	108.3 ± 0.3	0.024 ± 0.003	160.0	25.26 ± 0.10	0.40 ± 0.02	110.7 ± 1.5	0.044 ± 0.014
79.6	22.67 ± 0.02	0.48 ± 0.02	109.3 ± 0.3	0.019 ± 0.003	161.2	25.19 ± 0.08	0.41 ± 0.01	110.0 ± 1.0	0.003 ± 0.011
80.8	22.76 ± 0.01	0.47 ± 0.02	109.8 ± 0.3	0.025 ± 0.004	162.4	25.44 ± 0.10	0.39 ± 0.02	109.3 ± 2.1	−0.003 ± 0.019
82.0	22.85 ± 0.01	0.45 ± 0.02	108.2 ± 0.3	0.009 ± 0.004	163.6	25.66 ± 0.12	0.35 ± 0.03	107.4 ± 3.1	−0.041 ± 0.029
83.2	22.92 ± 0.02	0.44 ± 0.01	108.9 ± 0.4	0.011 ± 0.004					

Table 12. Surface photometry of NGC 7782.

r [″] (1)	μ_V [mag arcsec^{-2}] (2)	ϵ (3)	PA [°] (4)	$\cos 4\theta$ (5)	r [″] (6)	μ_V [mag arcsec^{-2}] (7)	ϵ (8)	PA [°] (9)	$\cos 4\theta$ (10)
1.2	18.75 ± 0.04	0.18 ± 0.01	4.5 ± 1.3	0.003 ± 0.005	43.2	22.42 ± 0.10	0.50 ± 0.01	175.0 ± 0.2	−0.025 ± 0.003
2.4	19.23 ± 0.04	0.24 ± 0.01	179.9 ± 0.9	0.007 ± 0.003	44.4	22.51 ± 0.11	0.50 ± 0.02	174.3 ± 0.2	−0.018 ± 0.002
3.6	19.65 ± 0.03	0.26 ± 0.01	176.3 ± 0.5	−0.003 ± 0.002	45.6	22.65 ± 0.12	0.48 ± 0.02	174.4 ± 0.3	0.004 ± 0.003
4.8	20.00 ± 0.03	0.29 ± 0.01	178.3 ± 0.4	−0.008 ± 0.002	46.8	22.73 ± 0.13	0.48 ± 0.01	174.9 ± 0.3	0.004 ± 0.003
6.0	20.29 ± 0.03	0.31 ± 0.01	0.9 ± 0.3	−0.008 ± 0.002	48.0	22.79 ± 0.14	0.49 ± 0.02	175.6 ± 0.3	0.007 ± 0.003
7.2	20.52 ± 0.03	0.34 ± 0.01	1.3 ± 0.3	−0.008 ± 0.002	49.2	22.88 ± 0.15	0.48 ± 0.01	176.6 ± 0.4	0.004 ± 0.004
8.4	20.71 ± 0.03	0.36 ± 0.01	1.7 ± 0.4	−0.014 ± 0.003	50.4	22.94 ± 0.15	0.49 ± 0.02	177.2 ± 0.4	0.012 ± 0.003
9.6	20.83 ± 0.03	0.37 ± 0.01	1.7 ± 0.7	−0.031 ± 0.004	51.6	23.01 ± 0.16	0.49 ± 0.01	178.1 ± 0.4	0.007 ± 0.003
10.8	20.95 ± 0.04	0.36 ± 0.01	1.8 ± 0.7	−0.032 ± 0.004	52.8	23.08 ± 0.18	0.48 ± 0.01	178.6 ± 0.3	0.014 ± 0.003
12.0	21.06 ± 0.04	0.22 ± 0.02	157.9 ± 2.3	−0.084 ± 0.008	54.0	23.14 ± 0.18	0.48 ± 0.01	178.3 ± 0.4	0.019 ± 0.003
13.2	21.09 ± 0.04	0.26 ± 0.01	152.0 ± 1.4	−0.017 ± 0.009	55.2	23.23 ± 0.20	0.48 ± 0.01	177.9 ± 0.4	0.021 ± 0.003
14.4	21.18 ± 0.04	0.26 ± 0.01	155.4 ± 1.1	0.002 ± 0.006	56.4	23.31 ± 0.22	0.47 ± 0.01	176.9 ± 0.4	0.023 ± 0.003
15.6	21.25 ± 0.04	0.27 ± 0.01	161.8 ± 0.9	0.011 ± 0.005	57.6	23.41 ± 0.23	0.47 ± 0.01	177.1 ± 0.4	0.020 ± 0.004
16.8	21.30 ± 0.04	0.30 ± 0.01	166.2 ± 0.8	0.001 ± 0.004	58.8	23.50 ± 0.25	0.47 ± 0.01	176.5 ± 0.4	0.016 ± 0.004
18.0	21.35 ± 0.05	0.32 ± 0.01	170.1 ± 0.7	−0.008 ± 0.003	60.0	23.59 ± 0.28	0.48 ± 0.01	176.5 ± 0.4	0.008 ± 0.004
19.2	21.42 ± 0.05	0.32 ± 0.01	171.7 ± 1.0	−0.022 ± 0.005	61.2	23.66 ± 0.29	0.48 ± 0.01	175.9 ± 0.5	0.010 ± 0.005
20.4	21.53 ± 0.05	0.27 ± 0.01	174.7 ± 1.4	−0.001 ± 0.008	62.4	23.69 ± 0.30	0.48 ± 0.01	175.9 ± 0.5	0.010 ± 0.005
21.6	21.56 ± 0.06	0.30 ± 0.01	174.7 ± 1.5	−0.026 ± 0.014	63.6	23.74 ± 0.32	0.48 ± 0.01	174.7 ± 0.4	0.007 ± 0.004
22.8	21.62 ± 0.06	0.30 ± 0.02	174.7 ± 2.2	−0.090 ± 0.012	64.8	23.80 ± 0.33	0.49 ± 0.01	174.4 ± 0.4	−0.000 ± 0.004
24.0	21.64 ± 0.06	0.33 ± 0.02	174.7 ± 2.3	−0.116 ± 0.014	66.0	23.81 ± 0.34	0.49 ± 0.01	173.3 ± 0.3	−0.004 ± 0.003
25.2	21.60 ± 0.08	0.38 ± 0.02	160.7 ± 2.3	−0.060 ± 0.023	67.2	23.85 ± 0.35	0.49 ± 0.01	172.7 ± 0.2	−0.014 ± 0.003
26.4	21.63 ± 0.07	0.40 ± 0.02	163.3 ± 2.0	−0.072 ± 0.022	68.4	23.87 ± 0.35	0.50 ± 0.01	172.2 ± 0.2	−0.017 ± 0.003
27.6	21.63 ± 0.07	0.41 ± 0.02	167.2 ± 2.1	−0.102 ± 0.020	69.6	23.95 ± 0.38	0.50 ± 0.01	171.9 ± 0.2	−0.013 ± 0.003
28.8	21.63 ± 0.07	0.45 ± 0.02	168.0 ± 1.7	−0.092 ± 0.018	70.8	24.11 ± 0.44	0.48 ± 0.01	171.5 ± 0.3	−0.010 ± 0.003
30.0	21.65 ± 0.07	0.46 ± 0.02	169.7 ± 1.3	−0.081 ± 0.013	72.0	24.25 ± 0.50	0.47 ± 0.01	171.8 ± 0.3	−0.004 ± 0.004
31.2	21.68 ± 0.07	0.47 ± 0.01	171.8 ± 1.0	−0.072 ± 0.011	73.2	24.39 ± 0.57	0.46 ± 0.01	172.6 ± 0.4	−0.009 ± 0.005
32.4	21.77 ± 0.07	0.47 ± 0.01	173.3 ± 0.8	−0.050 ± 0.008	74.4	24.51 ± 0.64	0.45 ± 0.01	172.3 ± 0.4	−0.003 ± 0.004
33.6	21.89 ± 0.07	0.46 ± 0.01	175.8 ± 0.5	−0.029 ± 0.005	75.6	24.59 ± 0.69	0.45 ± 0.01	173.3 ± 0.6	−0.001 ± 0.006
34.8	21.95 ± 0.07	0.46 ± 0.01	177.5 ± 0.3	−0.025 ± 0.004	76.8	24.57 ± 0.68	0.47 ± 0.01	173.0 ± 0.5	0.004 ± 0.006
36.0	22.01 ± 0.07	0.47 ± 0.01	178.3 ± 0.3	−0.018 ± 0.003	78.0	24.66 ± 0.73	0.46 ± 0.01	173.4 ± 0.5	0.005 ± 0.006
37.2	22.09 ± 0.07	0.48 ± 0.01	178.6 ± 0.3	−0.015 ± 0.003	79.2	24.78 ± 0.82	0.45 ± 0.01	173.4 ± 0.6	0.004 ± 0.007
38.4	22.17 ± 0.08	0.48 ± 0.01	178.2 ± 0.2	−0.009 ± 0.003	80.4	24.80 ± 0.84	0.46 ± 0.01	172.3 ± 0.5	−0.003 ± 0.005
39.6	22.23 ± 0.08	0.49 ± 0.01	177.7 ± 0.2	−0.011 ± 0.002	81.6	24.94 ± 0.95	0.46 ± 0.01	172.3 ± 0.7	−0.008 ± 0.008
40.8	22.28 ± 0.09	0.49 ± 0.01	176.7 ± 0.2	−0.017 ± 0.002	82.8	24.99 ± 0.99	0.46 ± 0.01	172.3 ± 0.6	−0.006 ± 0.008
42.0	22.34 ± 0.09	0.50 ± 0.01	175.6 ± 0.2	−0.022 ± 0.002					

3.3 Narrow-band imaging

The narrow-band Hα imaging of NGC 772, 3898 and 7782 was performed at the VATT in the same observing runs, during which we obtained the *V*-band images.

For each galaxy we obtained at least two emission-band and two continuum-band images, using the set of interference filters kindly provided by R. C. Kennicutt. The emission-band images were taken with three different interference filters ($\lambda_c = 6630$ Å, $\lambda_c = 6580$ Å, and $\lambda_c = 6680$ Å, respectively, for NGC 772, 3898 and 7782; $\Delta\lambda_{FWHM} = 70$ Å) in order to isolate the spectral region characterized by the redshifted Hα and [N II] ($\lambda\lambda$6548.0, 6583.4 Å) emission lines according to galaxy systemic velocity. The continuum-band images were taken through an interference filter ($\lambda_c = 6450$ Å; $\Delta\lambda_{FWHM} = 70$ Å), which has been selected to observe an emission-free spectral region sufficiently near to that of the emission-band filters in order to subtract off the stellar continuum in the emission-band images. Duration, date and filter of all the in-band and off-band exposures are collected in Table 3. Flat-field exposures of the twilight sky were taken at dawn and sunset for each filter.

The narrow-band images of the target galaxies were bias-subtracted, flat-field-corrected, aligned, averaged and cleaned of cosmic ray events in the same way as for the broad-band images. As a result of this standard data reduction, we obtained for each galaxy a single emission-band image and a single continuum-band image. The seeing FWHMs of these images as measured by fitting a two-dimensional Gaussian to the field stars are listed in Table 3. For each galaxy the best-seeing image was convolved with a Gaussian PSF to yield the same PSF FWHM of the worst-seeing image. Finally, the continuum-band image was suitably scaled and subtracted from the emission-band image to obtain a continuum-free map of the Hα + [N II] emission of the galaxy. The scalefactor for the continuum-band image was estimated by comparing the intensity a large number of field stars in the two bandpasses. The resulting continuum-band and continuum-free images of NGC 772, 3898 and 7782 are given in Sections 5.1.3, 5.2.3 and 5.3.3.

4 STRUCTURE MODELS

In order to describe the mass structure of each galaxy, we have to take advantage of both the photometric and kinematic data available.

We describe each galaxy by the superposition of two different components, namely a bulge and a disc. Both the components are assumed to be oblate, with the isodensity surfaces being similar concentric spheroids. In this framework, what we call a 'disc' is in fact a spheroidal component with a very high ellipticity, which we assume to be constant with radius.

Once the luminosity density parameters are constrained by the photometry (Section 4.1), we use the kinematics to evaluate the mass-to-light ratios and to discuss the gas-velocity distribution.

4.1 Photometric decomposition

Conventional bulge–disc photometric decompositions based on elliptically averaged surface-brightness profiles are subject to strong systematic errors due to the different intrinsic shapes of bulge and disc, and to the viewing angle of the galaxy (see Byun & Freeman 1995 for an extensive discussion). For this reason we applied to the *V*-band images of NGC 772, 3898 and 7782 a two-dimensional parametric decomposition technique. The bulge and disc photometric parameters used as the initial trial in modelling the observed kinematics were derived by fitting directly the galaxy surface-brightness distributions. Our decomposition method is based on the technique developed by Byun & Freeman, which we improved by introducing convolution with the seeing PSF and by weighting the observed surface brightness measured in each pixel according to the associated Poissonian noise and CCD readout noise.

4.1.1 Two-dimensional bulge–disc parametric decomposition

We assumed the galaxy surface-brightness distribution to be the sum of the contributions of an oblate bulge and an infinitely thin disc. We adopted the $r^{1/4}$ law (de Vaucouleurs 1948) to describe the surface brightness of the bulge component

$$I_{\rm bulge}(x,y) = I_{\rm e} \exp\left[-7.67\left\{\left(\frac{\sqrt{x^2+y^2(b/a)^{-2}_{\rm bulge}}}{r_{\rm e}}\right)^{1/4}-1\right\}\right], \quad (1)$$

where $I_{\rm e}$ and $r_{\rm e}$ are respectively the effective surface brightness and effective radius of the bulge. x and y are the apparent distances from galactic centre along the major and minor axis, and $(b/a)_{\rm bulge}$ is the apparent axial ratio of bulge. Bulge isophotes are ellipses with constant apparent ellipticity $\epsilon_{\rm bulge} = 1 - (b/a)_{\rm bulge}$.

The disc component is assumed to have an exponential surface brightness (Freeman 1970)

$$I_{\rm disc}(x,y) = I_0 \exp\left[\frac{\sqrt{x^2+y^2(b/a)^{-2}_{\rm disc}}}{h}\right], \quad (2)$$

where μ_0 and h are respectively the disc central surface brightness and scalelength, x and y are the apparent distances from galactic centre along the major and minor axes, and $(b/a)_{\rm disc}$ is the apparent axial ratio of disc. Disc isophotes are ellipses with constant apparent ellipticity $\epsilon_{\rm disc} = 1 - (b/a)_{\rm disc}$, and the disc inclination is $i = \arccos(b/a)_{\rm disc}$.

To derive the photometric parameters of the bulge [$I_{\rm e}$, $r_{\rm e}$ and $(b/a)_{\rm bulge}$] and the disc [I_0, h and $(b/a)_{\rm disc}$], we fitted iteratively a model of the surface brightness to the observations using a non-linear χ^2 minimization based on the Levenberg–Marquardt method (e.g. Bevington & Robinson 1992; Press et al. 1996).

The galaxy centre, and the bulge and disc position angles, as well as the sky level, are not free parameters in our decomposition. The galaxy centre is assumed to be the mean centre of the ellipses which fit the galaxy isophotes. Bulge and disc are assumed to have the same position angle, which is the mean value of the major-axis position angle of ellipses which fit the galaxy isophotes. The sky level is estimated as described in Section 3. The seeing effects were taken into account by convolving the model image with a circular Gaussian PSF with the FWHM measured using the stars in the image (Table 3). The convolution was performed as a product in Fourier domain before the χ^2 minimization.

For each pixel (x, y), the observed galaxy photon counts $\mathcal{I}_{\rm gal}$ are compared with those predicted from the model $\mathcal{I}_{\rm bulge} + \mathcal{I}_{\rm disc}$. Each pixel is weighted according to the variance of its total observed photon counts due to the contribution of both galaxy and sky, and determined assuming photon noise limitation. Therefore we can write

$$\chi^2 = \sum_{x=1}^{N}\sum_{y=1}^{M} \frac{[\mathcal{I}_{\rm mod}(x,y) - \mathcal{I}_{\rm gal}(x,y)]^2}{\mathcal{I}_{\rm gal}(x,y) + \mathcal{I}_{\rm sky}(x,y)}, \quad (3)$$

with x and y ranging over the whole $N \times M$ pixel image.

To derive the six free parameters of the model surface-brightness distribution, we adopted as the initial trial for χ^2 minimization the values obtained by performing a standard photometric decomposition with a parametric technique similar to that adopted by Kent (1985). In fact, we decomposed the observed surface-brightness profile along both the major axis (obtained by fitting ellipses to isophotes) and the minor axis (obtained from the major-axis profile scaled by the factor $1 - \epsilon$) as the sum of an $r^{1/4}$ oblate bulge plus an exponential infinitely thin disc. To take into account the seeing effect, we truncated the major- and minor-axis profiles at a radius corresponding to a couple of PSF FWHM from the centre. We assumed the minor-axis profiles of bulge and disc to be the same as the major-axis profile scaled respectively by a factor $1 - \epsilon_{\rm bulge} = (b/a)_{\rm bulge}$ and $1 - \epsilon_{\rm disc} = (b/a)_{\rm disc}$. A least-squares fit of the model to the photometric data provided the values of $I_{\rm e}$, $r_{\rm e}$, $(b/a)_{\rm bulge}$, I_0, h and $(b/a)_{\rm disc}$ to be used as the initial trial parameters for the two-dimensional photometric decomposition.

The photometric parameters of the bulge and the disc obtained for NGC 772, 3898 and 7782 are given in Table 13. The model

Table 13. Parameters from the bulge–disc photometric decomposition.

Object	Bulge				Disc					Fit[a]
	$\mu_{\rm e}$ [mag arcsec^{-2}]	$r_{\rm e}$ [″]	$r_{\rm e}$ [kpc]	$(b/a)_{\rm bulge}$	μ_0 [mag arcsec^{-2}]	h [″]	h [kpc]	$(b/a)_{\rm disc}$	i [°]	
NGC 772	22.7	60.5	10.2	0.66	21.5	96.3	16.2	0.39	67	1D
	22.8	65.4	11.0	0.77	21.3	67.0	11.3	0.62	52	2D
NGC 3898	20.9	25.6	2.1	0.64	21.6	45.9	3.8	0.37	68	1D
	20.6	18.9	1.6	0.71	20.4	29.0	2.4	0.52	59	2D
NGC 7782[b]	20.2	3.6	1.3	0.85	20.5	23.3	8.5	0.41	66	1D
	19.9	2.9	1.1	0.71	20.3	21.6	7.8	0.56	56	2D

[a] 1D = parametric fit on the ellipse-averaged profiles; 2D = two-dimensional parametric fit.
[b] For NGC 7782 the best fit to the observed surface-brightness distribution has been obtained adopting an exponential bulge (see discussion in Section 5.3.4).

surface brightnesses obtained for the sample galaxies are discussed in Sections 5.1.2, 5.2.2 and 5.3.2.

4.1.2 Test with model galaxies

To test the reliability and accuracy of our two-dimensional technique for bulge–disc photometric decomposition, we applied the decomposition program to a set of artificial disc galaxies. We generated 100 images of galaxies with an $r^{1/4}$ oblate bulge plus an exponential infinitely thin disc. The scale surface-brightness, scalelength, and apparent axial ratios of bulge and disc of the artificial galaxies were randomly chosen in the range of values observed by Kent (1985) for a large sample of S0 and spiral galaxies. The adopted ranges are

$$18 \leq \mu_{\rm e} \leq 24\,{\rm mag\,arcsec^{-2}}, \tag{4}$$

$$3 \leq r_{\rm e} \leq 10\,{\rm kpc}, \tag{5}$$

$$0.6 \leq (b/a)_{\rm bulge} \leq 1 \tag{6}$$

for the bulge parameters, and

$$19 \leq \mu_{\rm e} \leq 23\,{\rm mag\,arcsec^{-2}}, \tag{7}$$

$$3 \leq r_{\rm e} \leq 15\,{\rm kpc}, \tag{8}$$

$$0.2 \leq (b/a)_{\rm disc} \leq 1 \tag{9}$$

for the disc parameters. The parameters of the artificial galaxies have also to satisfy the following conditions

$$(b/a)_{\rm disc} < (b/a)_{\rm bulge}, \tag{10}$$

$$0 < B/T < 0.8. \tag{11}$$

All the simulated galaxies were assumed to be at the Virgo cluster distance ($d = 17$ Mpc; Freedman et al. 1994), corresponding to a scale of $82.4\,{\rm pc\,arcsec^{-1}}$. The pixel scale used was $0.4\,{\rm arcsec\,pixel^{-1}}$, and the CCD gain and readout noise were respectively $1.4\,{\rm e^-\,ADU^{-1}}$ and $6.5\,{\rm e^-}$ in order to simulate the VATT observations. We fixed the seeing FWHM at 2.0 arcsec. We added a sky background level of $10\,{\rm count\,pixel^{-1}}$, which corresponds to a sky surface brightness of $21.8\,{\rm mag\,arcsec^{-2}}$ in the *V*-band, adopting the absolute calibration derived from our real observations. This is a typical surface brightness value for a dark sky as reported by Binney & Merrifield (1998). An appropriate level of noise was added to the resulting image to yield a signal-to-noise ratio similar to that of the photometric data we obtained for NGC 772, 3898 and 7782 during the VATT observing runs.

The images of the artificial galaxies have been analysed as if they were real. The two-dimensional parametric decomposition has been applied using as initial trial parameters the $I_{\rm e}$, $r_{\rm e}$, $(b/a)_{\rm bulge}$, I_0, h, and $(b/a)_{\rm disc}$ values obtained with a standard parametric decomposition of the major- and minor-axis surface brightness profiles measured by fitting ellipses to the galaxy isophotes. The fitting algorithm was able to recover the input parameters within the estimated errors with a scatter consistent with the results of the similar double-blind tests performed by Schombert & Bothun (1987), Byun & Freeman (1995) and Wadadekar, Robbason & Kembhavi (1999).

4.2 Dynamical models

In order to investigate the gas and stellar kinematics, we use the self-consistent dynamical models by Pignatelli & Galletta (1999). We give here just a brief summary of the technique itself and of the general assumptions used.

The galaxy can be described by superposition of different components. For each component, we separately assume that:

(1) the density distribution is oblate, without triaxial structures;
(2) the isodensity surfaces are similar concentric spheroids;
(3) the surface density profile follows a simple $r^{1/4}$ or an exponential law;
(4) the velocity distribution is locally Gaussian;
(5) the velocity dispersion is isotropic ($\sigma_r = \sigma_\theta = \sigma_z$), and
(6) the mass-to-light ratio is constant with radius.

Our model does not consider the possible presence of triaxial structures (bar; triaxial bulge; tilted component; warp) or of anisotropy in the velocity distribution (with predominance of radial or tangential orbits).

With these assumptions, the model has $4n + 1$ free parameters, where n is the number of adopted components: namely the luminosity $L_{\rm tot}$, scalelength ($r_{\rm e}$ or h), mass-to-light ratio M/L and flattening b/a of each component plus the inclination angle of the galaxy. In principle, photometry can be used (as explained in Section 4.1) to constrain all these parameters except the mass-to-light ratios and the inclination angle i, which must be derived by kinematics.

For each given choice of the parameters above, we compute the gravitational potential of the total mass distribution and integrate the Jeans equations for the stellar component, obtaining a self-consistent model of the rotation velocity and velocity-dispersion profiles which include the asymmetric drift effects.

In order to compare the observed data with the prediction of the model, we also need to reproduce the deviations of the LOSVD profiles from a pure Gaussian shape. In fact, in the regions where the bulge and disc luminosities are comparable we expect that the superposition of the rapid rotation of the disc with the slower rotation of the other components will produce a clearly non-Gaussian, and sometimes even double-peaked, LOSVD even assuming that each individual component has a Gaussian velocity distribution.

We parametrized these deviations in terms of the usual Gauss–Hermite series higher moments h_3 and h_4, which we obtained by means of a first-order approximation from the momenta of the model velocity distribution (van der Marel & Franx 1993; Pignatelli & Galletta 1999).

Finally, we convolved the results of the model with the seeing and took into account the instrumental set-up used in the different observations (slit width, pixel size). The final model profiles are compared with the observed stellar kinematic data and the best-fitting model is found with the help of the standard reduced χ^2-analysis. Masses and mass-to-light ratios of different components are given in Table 14.

Once the fit of the stellar kinematics has been performed, and the overall potential of the galaxy is known, one can derive the circular velocity $V_{\rm c} = R(\partial\Phi/\partial R)$ directly. By overlaying the $V_{\rm c}$ obtained in this way (and corrected for inclination) on the observed gas rotation velocity, we can immediately notice any deviation from purely circular motion. The evaluation of the different convolution effects is crucial especially within the innermost regions, where the rise of the velocity curve is smoothed, and the value of the velocity dispersion is increased, by the seeing effects.

Table 14. Parameters from the dynamical models.

Object	Bulge				Disc				Dark halo	Bulge + Disc	
	L^a [%]	L^b [$L_{\odot,V}$]	M^c [$M_\odot$]	M/L [$\Upsilon_\odot$]	L^a [%]	L^b [$L_{\odot,V}$]	M^c [$M_\odot$]	M/L [$\Upsilon_\odot$]	M^d [$M_\odot$]	M^b [$M_\odot$]	M/L [$\Upsilon_\odot$]
NGC 772	52%	5.8×10^{10}	3.8×10^{11}	6.6	48%	5.4×10^{10}	1.8×10^{11}	3.3	–	5.6×10^{11}	5.0
NGC 3898	67%	1.1×10^{10}	7.1×10^{10}	6.4	33%	4.8×10^{9}	2.0×10^{10}	4.2	9.0×10^{9}	9.1×10^{10}	5.8
NGC 7782	11%	1.03×10^{10}	8.5×10^{10}	8.3	89%	8.6×10^{10}	3.6×10^{11}	4.2	–	4.4×10^{11}	4.6

[a] from the 2D decomposition in Table 13.
[b] adopting the total corrected *V*-band luminosities $L^0_{V_T}$ derived from Table 1.
[c] from the dynamical models shown in Figs 7, 15 and 20.
[d] at the outermost observed radius measured for the ionized-gas component.

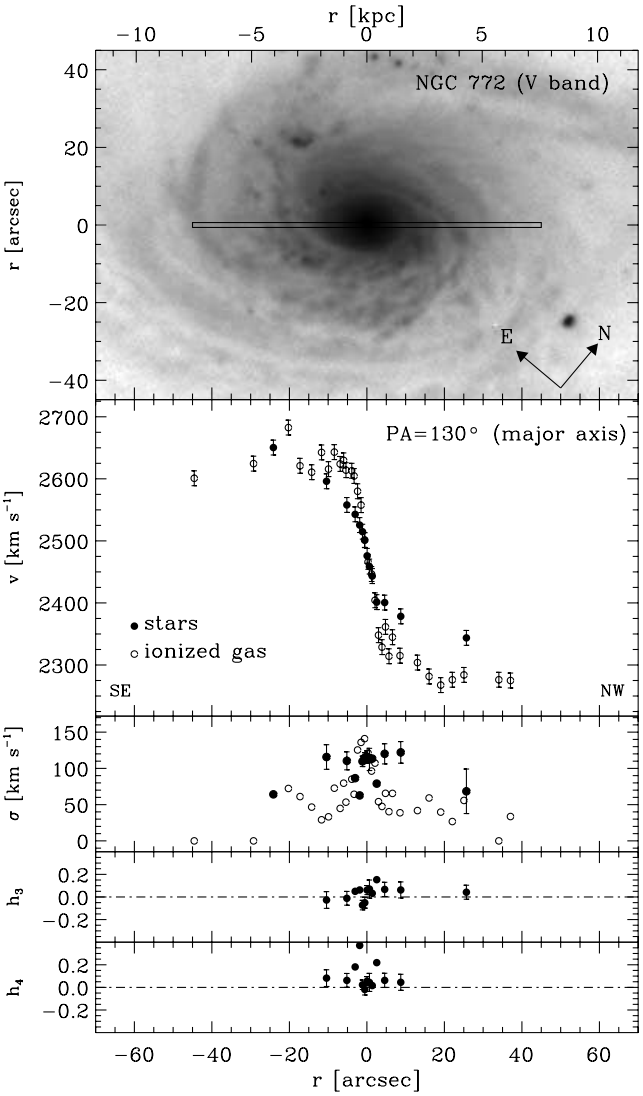

Figure 2. The stellar (*filled circles*) and ionized-gas (*open circles*) kinematics measured along the major axis (PA = 130°) of NGC 772.

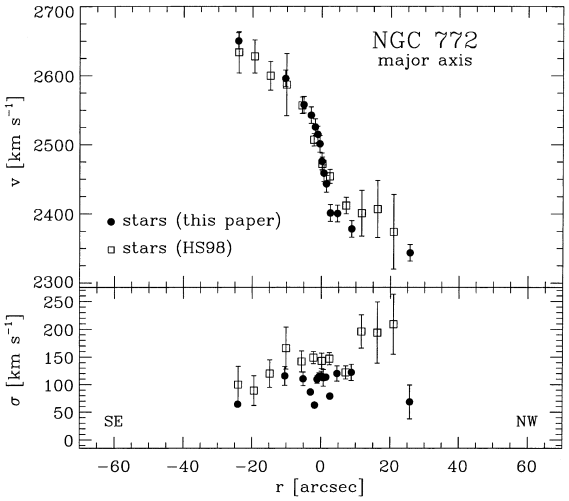

Figure 3. NGC 772 major-axis stellar kinematics. The stellar kinematics derived in the present study at PA = 130° (*filled circles*) are shown superimposed on those obtained by Heraudeau & Simien (1998) at PA = 131° (*open squares*).

5 RESULTS

5.1 NGC 772

5.1.1 Stellar and ionized-gas kinematics

The stellar kinematic data extend to more than 30 arcsec (5.0 kpc) on the receding side of NGC 772, and to about 24 arcsec (4.0 kpc) on its approaching side (Fig. 2). In the inner 4 arcsec (0.7 kpc), the rotation velocity of stars increases to 80 km s^{-1}. At larger radii, it rises more gently out to 120 km s^{-1} at the last measured point. At the centre the stellar velocity dispersion shows a maximum of about 120 km s^{-1}; away from the nucleus it falls off to 75 km s^{-1} at 4 arcsec. Outside it remains high, ranging between 90 and 140 km s^{-1}.

The stellar velocity curve and velocity-dispersion profile we measured along the major axis of NGC 772 are compared in Fig. 3 to those obtained by Heraudeau & Simien (1998). The two data sets cover almost the same radial region, and have been collected along two close position angles (PA = 130° and 131°). Our line-of-sight velocities agree within the errors with those measured by Heraudeau & Simien (1998). However, their velocity dispersions are higher than those we found. This is simply due to the different technique adopted in measuring the stellar kinematic parameters rather than to real kinematic features observed at the two different position angles.

The ionized-gas velocity is measured out to 45 arcsec (7.6 kpc) on the receding side and to less than 40 arcsec (6.7 kpc) on the approaching side (Fig. 2). The ionized-gas rotation velocity has a steeper gradient than the stellar velocity, reaching a value of 140 km s^{-1} at $|r| \simeq 5$ arcsec (0.8 kpc), increasing to 175 km s^{-1} at $|r| \simeq 10$ arcsec (1.7 kpc) and then flattening out. The gas velocity dispersion strongly peaks to about 150 km s^{-1} in the centre; it drops rapidly to values lower than 50 km s^{-1} for $|r| \gtrsim 5$ arcsec.

5.1.2 *V-band surface photometry and bulge–disc decomposition*

The *V*-band ellipse-averaged radial profiles of surface brightness, ellipticity, position angle and $\cos 4\theta$ Fourier coefficient of NGC 772 have been measured out to 229 arcsec (38.5 kpc) from the centre (Fig. 4).

In the inner 60 arcsec (10.1 kpc) the values of ellipticity and position angle show a series of bumps and wiggles, oscillating between 0.15 and 0.36 and between 98° and 143°, respectively. These features are due to the inner spiral arms of the galaxy. The bump in the surface-brightness profile at 90 arcsec, and the corresponding abrupt variations in the position angle and fourth-order cosine Fourier coefficient can be ascribed to the prominent northern arm (see Fig. 5). At larger radii, the galaxy light is dominated by the contribution of the disc component characterized by an exponential

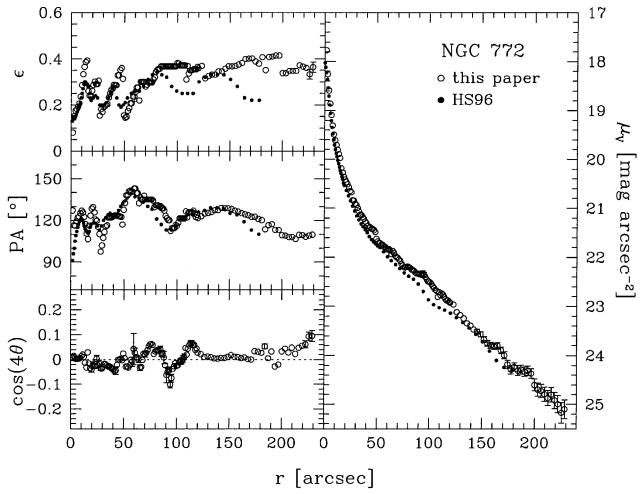

Figure 4. The *V*-band surface-brightness, ellipticity, position angle and $\cos 4\theta$ coefficient profiles we measured as a function of the semimajor axis length for NGC 772 (*open circles*). Error bars smaller than symbols are not plotted. The *V*-band surface brightness, ellipticity and position angle profile from Heraudeau & Simien (1996, *filled circles*) are also plotted.

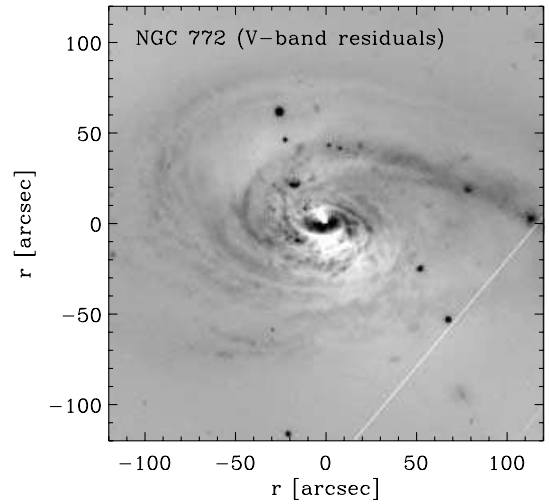

Figure 5. The residual image of NGC 772 obtained by subtracting the model surface brightness to the observed one. The orientation of the image is the same as that of Fig. 2. The photometric parameters of the model are given in Table 13.

surface-brightness profile and almost constant ellipticity ($\epsilon \simeq 0.35$) and position angle (PA $\simeq 120°$).

In Fig. 4 our data are compared to those obtained by Heraudeau & Simien (1996) in the same band. The photometric profiles of Heraudeau & Simien (1996) extend out to 180 arcsec from the centre, and their surface brightness is $\lesssim$0.4 mag arcsec^{-2} fainter than ours. In the inner 50 arcsec their position angle and ellipticity data have smoother radial trends than those we measured. We noticed that the position-angle values included by Heraudeau & Simien (1996) in table 5 of their paper differ from those they plotted in their fig. 10. In our comparison we adopted the plotted ones. The disagreement between the two sets of data can be explained if the tabulated values result from an isophotal ellipse-fitting performed on an image of NGC 772 with an incorrect orientation.

In Fig. 5 we show the result of the bulge–disc photometric decomposition of the surface-brightness distribution of NGC 772, which has been performed with the parametric two-dimensional technique discussed in Section 4.1. The spiral arms extending into the very centre of NGC 772 are clearly visible in the residual image obtained by subtracting the model surface brightness of the galaxy from the observed surface brightness. These structures resemble those detected by Carollo et al. (1997) and Carollo, Stiavelli & Mack (1998) in several Sa – Sbc galaxies, in which the spiral pattern is visible down to the innermost radius accessible to the HST WFPC2 imaging.

By fitting an exponential profile to the ellipse-averaged surface-brightness profile of NGC 772 measured in the *B* band, Lu (1998) derived the following disc parameters $\mu_0 = 22.01$ mag arcsec^{-2}, $h = 72.4$ arcsec and $b/a = 0.58$. Our exponential disc results larger ($h = 96.3$ arcsec) and slightly more inclined ($b/a = 0.39$) than that obtained by Lu. This is due to the different decomposition technique we adopted more than to the different bandpass in which we observed. In fact, Lu fitted his exponential disc directly to the observed surface-brightness profile in the radial range between 75.1 and 133.1 arcsec (which he judged by eye to be disc-dominated) without taking into account any contribution from the conspicuous bulge component.

5.1.3 *Ionized-gas distribution*

In NGC 772 most of the H II regions visible in our Hα + [N II] image (Fig. 6) lie along the two arms, extending to the northern side of the galaxy, and along the short and double-ended arm opposite to them.

The ionized-gas emission is concentrated in the region of the galaxy ($r \lesssim 40$ arcsec) bounded by the pseudo-ring formed by the two tightly wound northern spiral arms. In the Hα + [N II] emission map it is possible to disentangle an outer region extending between 10 and 40 arcsec, and characterized by smooth and diffuse emission, from the inner region ($r \lesssim 10$ arcsec) characterized by more concentrated emission and contributing about 5 per cent of the total flux.

The ionized gas between 10 and 40 arcsec shows the kinematic behaviour typical of a disc ($V/\sigma \simeq 5$) as inferred from its high rotation velocity and low velocity dispersion (Fig. 2).

In the inner region the kinematic behaviour of the gas is different. The observed gas velocity dispersion (ranging between 70 and 150 km s^{-1}) is comparable to that of the stellar component, and therefore is far higher than that expected from thermal motion or small-scale turbulence ($\sigma \lesssim 50$ km s^{-1}) typically observed in a gaseous disc. This may well be an indication that in this region the

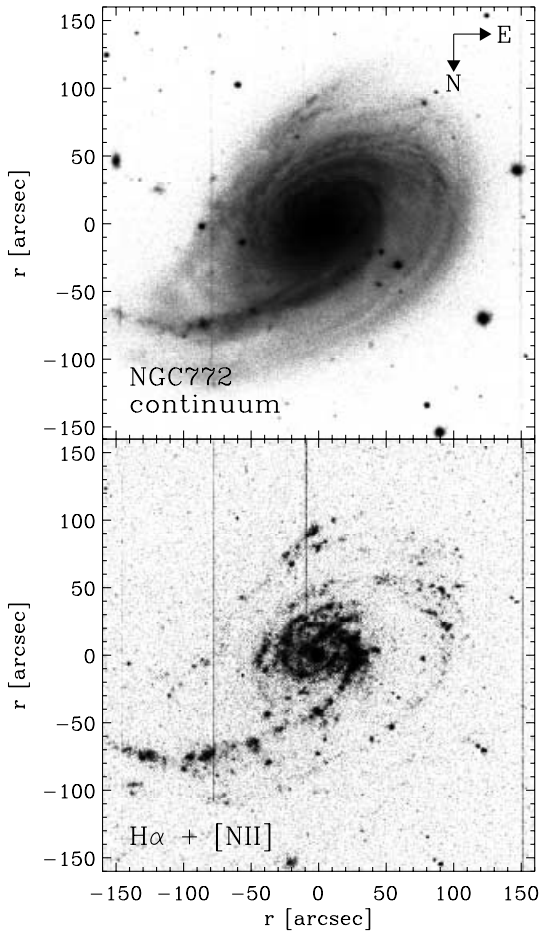

Figure 6. The stellar-continuum image (*upper panel*) and the continuum-subtracted Hα + [N II] emission image (*lower panel*) of NGC 772.

gas is being dynamically supported by pressure (i.e., random motions) rather than rotation, as it occurs in the outer part of the galaxy. There is, however, a wide region ($4 < r < 10$ arcsec) in which the gas velocity dispersion is still only marginally greater than 50 km s^{-1}, and appears to be lower than its stellar counterpart [see panel (b) in Fig. 7]. The high velocity dispersions observed near the nucleus could then only be an observational effect due to seeing. In order to discriminate between the two cases, the application of a dynamical model is required.

5.1.4 *Dynamical modelling*

In Fig. 7 we show for NGC 772 the comparison between the photometric and kinematic data and the best-fittting photometric dynamical models we obtained with the techniques discussed in Section 4. The mass-to-light ratios, flattening and masses of bulge and disc stellar components of NGC 772 derived with the dynamical modelling described in Section 4.2 are given in Table 14.

The agreement between the stellar kinematic data and the predictions of the dynamical model are fairly good at all radii, apart from the features observed in the LOSVD at $|r| \simeq 3$ arcsec. At this radius we notice a sharp decrease (from 115 to 80 km s^{-1}) in the observed velocity dispersion and very strong asymmetries in the line shape, while the rotation velocity does not show any significant variation. The model is unable to reproduce these abrupt but radially confined changes in the velocity-dispersion, h_3 and h_4 profiles. Either absorbing dust or nuclear peculiar motions could be responsible for this feature.

It is worth noting that the model reproduces the observed gaseous and stellar rotation velocity without the need of introducing a dark halo. According to the photometric decomposition, our kinematic data are limited to the bulge-dominated region of NGC 772 where the luminous mass is expected to dominate the galaxy dynamics. In agreement with these results, the dynamical model shows that asymmetric drift has a sizable effect on the stellar component in the whole observed region, as can be derived from the difference between the stellar rotation velocity and the circular speed (35 km s^{-1} at the farthest measured point).

Once the convolution with seeing and instrumental set-up has been taken into account, the gas appears to rotate in almost circular orbits. We conclude that the gas rotation curve of this galaxy can not be classified as a slowly rising one, and that the observed central rise in the gas velocity dispersion is due to seeing effects.

5.2 NGC 3898

5.2.1 *Stellar and ionized-gas kinematics*

The stellar kinematic parameters are observed out to 20 arcsec (1.7 kpc) and 30 arcsec (3.4 kpc) on the approaching and receding sides of NGC 3898, respectively (Fig. 8). The stellar rotation velocity increases linearly up to 130 km s^{-1} in the inner 10 arcsec (0.8 kpc), and then it decreases to 90 km s^{-1} at the last observed radius. At the centre, the stellar velocity dispersion is about 220 km s^{-1}, and then increases up to a maximum value of 240 km s^{-1} at $|r| \simeq 1$ arcsec (Fig. 9), suggesting the presence of an unresolved kinematically decoupled core component (see Friedli 1996 for a discussion about this feature in the velocity-dispersion profile). Off the nucleus, the stellar velocity dispersion decreases to 160 km s^{-1} on the approaching side and 130 km s^{-1} on the receding side.

The stellar velocity curve and velocity-dispersion profile measured along the major axis of NGC 3898 are compared in Fig. 9 to those obtained by Whitmore et al. (1984), Fillmore et al. (1986) and Heraudeau et al. (1999). Although the velocity data agree within the errors, a difference in the central velocity gradients measured by the various groups is present. In particular, there is a velocity discrepancy (ranging between 100 and 150 km s^{-1}) between our outer rotation velocities and those by Whitmore et al., who also measured a higher velocity dispersion on the receding side.

The ionized-gas kinematic parameters extend to 90 arcsec (7.5 kpc) on each side of the nucleus (Fig. 8). The gas rotation velocity has a steeper gradient than the stellar velocity, reaching 200 km s^{-1} at $|r| \simeq 10$ arcsec and remaining almost constant at this value further out. The gas velocity dispersion is about 90 km s^{-1} for $|r| \lesssim 10$ arcsec, decreasing at larger radii ($|r| \gtrsim 30$ arcsec) to 20 km s^{-1} on both sides of the nucleus.

The ionized-gas rotation curves we measured along the major axis of NGC 3898 from the spectra obtained with INT and MMT are compared in Fig. 10 to the Hα rotation velocities obtained by Rubin et al. (1985) and Fillmore et al. (1986). There is a good agreement between the line-of-sight velocities obtained in the different runs. In particular, all the rotation curves closely match each other, showing the same wiggles and bumps in the velocity

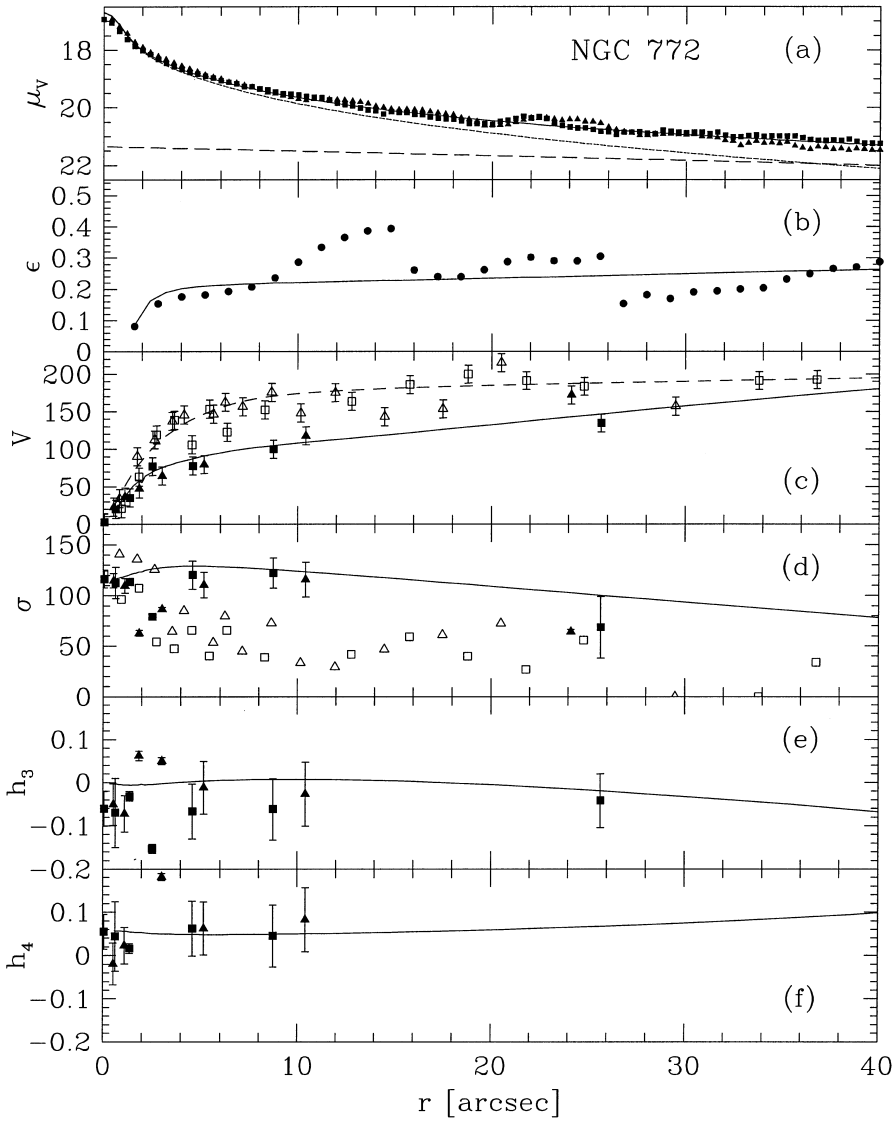

Figure 7. Photometric and dynamical radial profiles for NGC 772 with their respective best-fitting curves obtained from our models. **(a)** *V*-band surface brightness (*filled symbols*) as a function of radius along the major axis. We also plot the model bulge (*dotted line*) and disc (*dashed lines*) surface-brightness profiles, together with their sum convolved with the seeing (*solid line*). **(b)** Ellipse-averaged ellipticity for the *V*-band data (*filled circles*) and the photometric model (*solid line*). **(c)** Observed stellar velocity (*filled symbols*) with its associated model (*solid line*), and the ionized-gas velocity (*open symbols*). The *dashed line* is the circular velocity inferred from the dynamical model. **(d)** The same as (c), but for the velocity dispersion. **(e)** the same as (c), but for h_3 coefficients of the Gauss–Hermite expansion of the line profile of the stars. **(f)** The same as (c), but for h_4 coefficients of the Gauss–Hermite expansion of the line profile of the stars. In all the plots the *square symbols* and the *triangle symbols* represent data derived for the approaching NW side and for the receding SE side, respectively.

for $|r| < 8$ arcsec. However, between 8 and 20 arcsec on both sides of the nucleus Rubin et al. (1985) measured a slower rotation than either we or Fillmore et al. (1986) derived. As far as the gas velocity dispersion is concerned, only our own data are available. They are based on the linewidths of the [O III] λ5006.8 and Hα emission lines present in the MMT and INT spectra. The two data sets are consistent within the scatter of the points derived from the [O III] λ5006.8 line.

5.2.2 *V-band surface photometry and bulge–disc decomposition*

The *V*-band radial profiles of surface brightness, ellipticity, position angle and $\cos 4\theta$ Fourier coefficient measured by fitting ellipses to the NGC 3898 isophotes extend out to 164 arcsec (13.6 kpc) from the centre (Fig. 11).

The ellipticity rises from 0.23 to 0.39 in the inner 12 arcsec (1.0 kpc), remaining almost constant out to 40 arcsec (3.3 kpc). Between 40 and 110 arcsec (9.1 kpc) it increases to a maximum of 0.5 at 75 arcsec (6.2 kpc) and decreases to the initial value of 0.39. Further out it remains almost constant at 0.37 out to the farthest observed radius. The isophotal position angle is constant at 109° at all radii. The isophotes are slightly disky between 40 and 85 arcsec (7.1 kpc) and elliptical elsewhere. The surface-brightness profile is extremely regular, with a few small bumps due to the spiral arms.

In Fig. 11 our surface-brightness radial profile is compared to those obtained by Watanabe (1983), and Heraudeau & Simien (1996), who also measured for NGC 3898 the ellipticity and

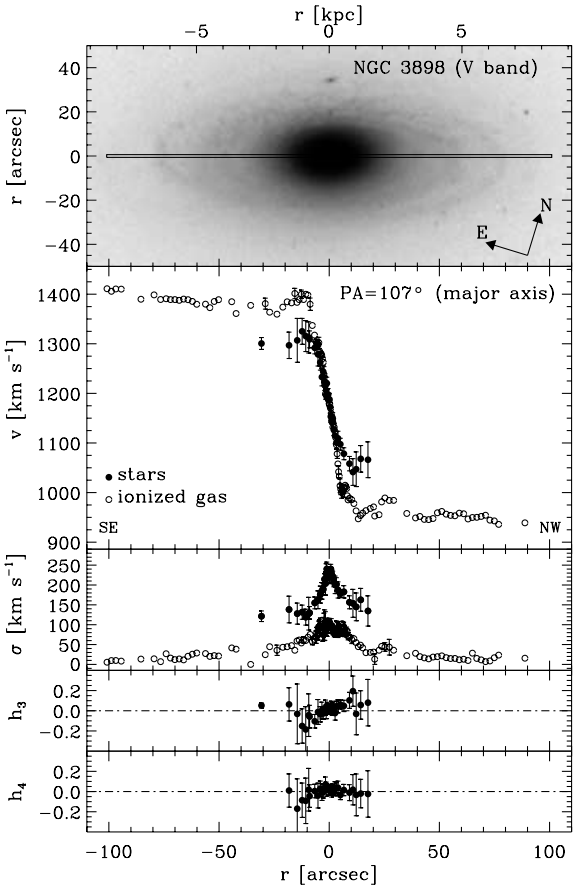

Figure 8. The stellar (*filled circles*) and ionized-gas (*open circles*) kinematic parameters measured along the major axis (PA = 107°) of NGC 3898.

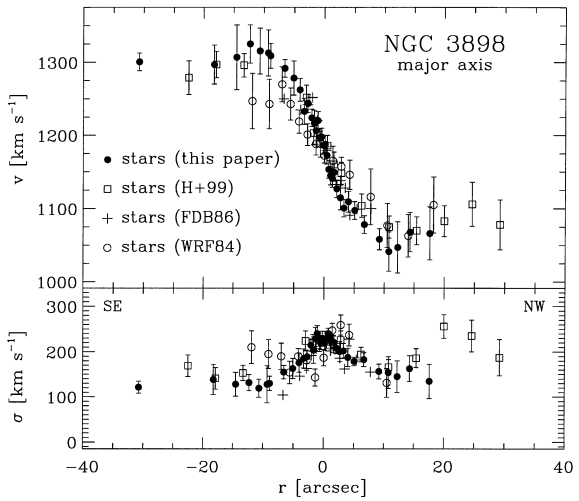

Figure 9. NGC 3898 major-axis stellar kinematic parameters. The stellar velocity and velocity dispersion derived in the present study at PA = 107° (*filled circles*) are shown superimposed on those obtained by Whitmore et al. (1984, *open circles*), Fillmore et al. (1986, *crosses*), and Heraudeau et al. (1999, *open squares*) for the same position angle.

position angle radial profiles. The agreement between our data and those of Heraudeau & Simien (1996) is good. The surface brightness measured by Watanabe in the radial region between 10 and 100 arcsec is $\lesssim$0.5 mag arcsec^{-2} fainter than ours. The

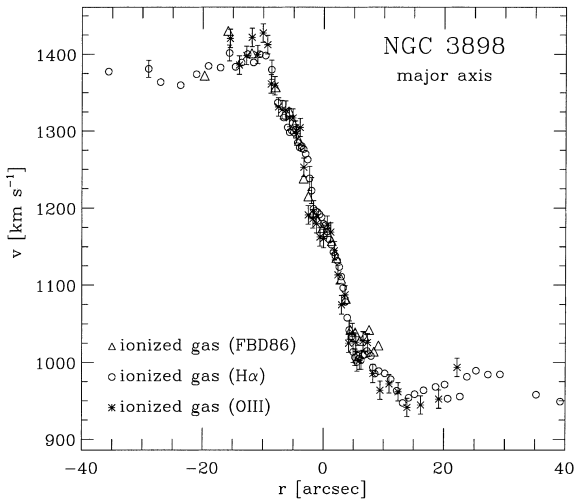

Figure 10. NGC 3898 major-axis ionized-gas kinematic parameters. The ionized-gas velocities derived in the present study at PA = 107° using the spectra obtained at INT (*open circles*) and MMT (*asterisks*) are shown superimposed on those obtained measuring the Hα emission line by Rubin et al. (1985, *crosses*) and Fillmore et al. (1986, *open triangles*) along the same position angle.

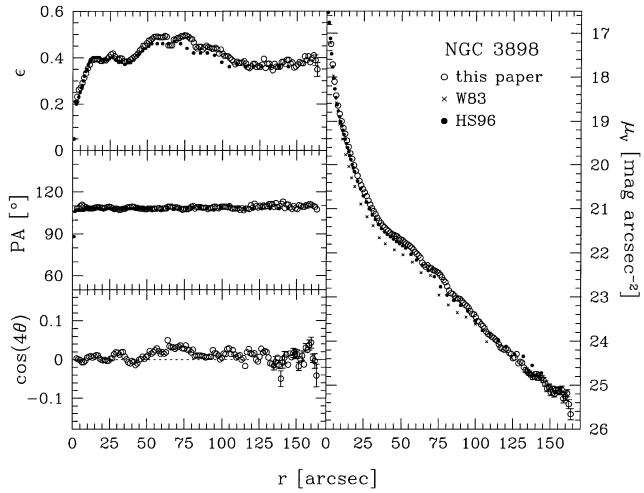

Figure 11. The *V*-band surface-brightness, ellipticity, position angle and cos 4θ coefficient profiles we measured as function of the semimajor axis length for NGC 3898 (*open circles*). Error bars smaller than symbols are not plotted. The *V*-band surface-brightness, ellipticity and position angle profiles from Heraudeau & Simien (1996, *filled circles*) and the surface-brightness profile by Watanabe (1983, *crosses*) are also shown.

surface-brightness profile of Kodaira et al. (1990) is not shown in Fig. 11. In their Photometric Atlas of Northern Bright Galaxies, only the profiles extracted along the major and minor axes of NGC 3898 are available, and there is not an ellipse-averaged profile. This is also true for NGC 7782.

The result of the two-dimensional bulge–disc parametric decomposition of the surface-brightness distribution of NGC 3898 is shown in Fig. 12. The spiral pattern shows up in the panel of the residuals, as well as a central structure due to the difference in this region between the observed ellipticity (increasing from 0.28 to 0.39) and the constant value ($\epsilon_{\rm bulge} = 0.39$) derived for the bulge component.

The surface-brightness profiles of Watanabe (1983) and Kodaira et al. (1990) were fitted with a $r^{1/4}$ bulge and an

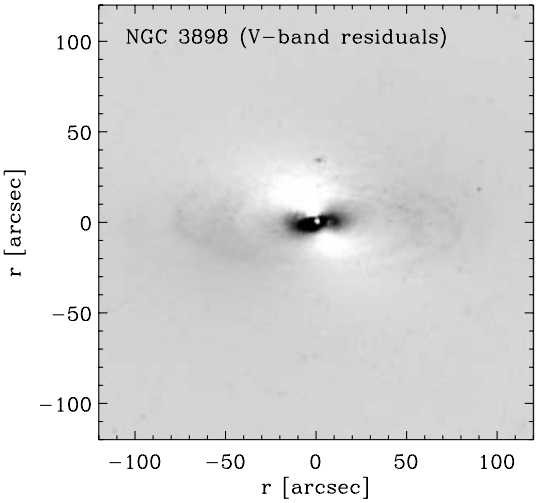

Figure 12. The residual image of NGC 3898 obtained by subtracting the model surface brightness from the observed one. The orientation of the image is the same as that of Fig. 8. The photometric parameters of the model are given in Table 13.

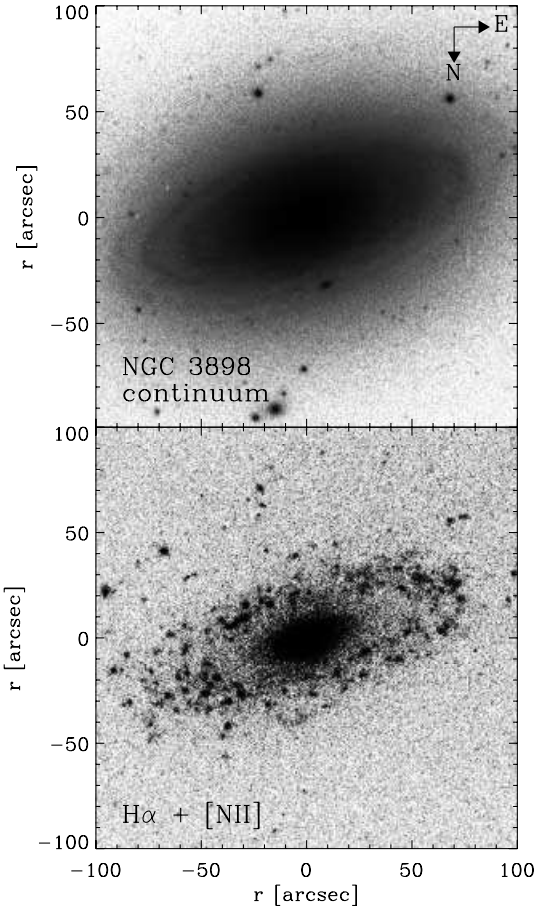

Figure 13. The stellar-continuum image (*upper panel*) and the continuum-subtracted Hα + [N II] emission image (*lower panel*) of NGC 3898.

exponential disc by van Driel & van Woerden (1994) and Baggett et al. (1998), respectively. Van Driel & van Woerden, using Burstein's (1979) method, obtained the following photometric parameters: $\mu_e = 17.1$ mag arcsec^{-2}, $r_e = 4.4$ arcsec, $\mu_0 = 20.6$ mag arcsec^{-2}, and $h = 33.0$ arcsec. The best-fitting parameters

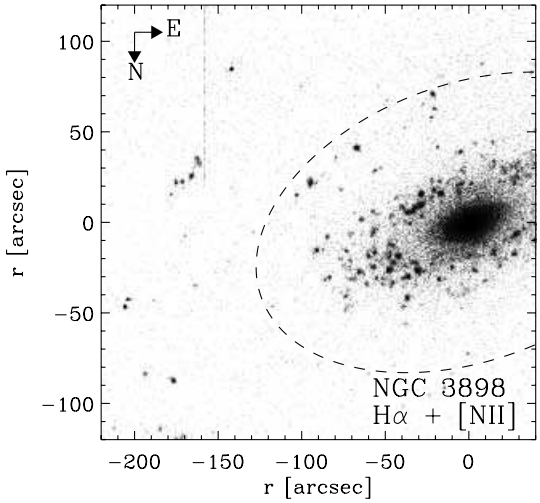

Figure 14. Continuum-subtracted Hα + [N II] emission image of NGC 3898, showing the H II regions tracing the two external faint arms of the galaxy. The *dashed line* indicates the optical size of the NGC 3898 corresponding to the D_{25} *B*-band diameter given in Table 1.

derived by Baggett et al., performing an intensity-weighted fit between 3 and 156 arcsec to avoid the portion of the profile most affected by seeing, are $\mu_e = 18.3$ mag arcsec^{-2}, $r_e = 6.2$ arcsec, $\mu_0 = 20.8$ mag arcsec^{-2}, and $h = 37.8$ arcsec. The results of van Driel & van Woerden and Baggett et al. are consistent if we take into account the fact that they used an ellipse-averaged profile and the profile extracted along the galaxy major axis, respectively. The bulge and disc scale parameters we obtained for NGC 3898 are quite different, since we have taken properly into account the apparent axial ratios of the two components.

5.2.3 *Ionized-gas distribution*

Ho, Filippenko & Sargent (1997) classified the nucleus of NGC 3898 as intermediate between an H II nucleus and a LINER. This bright nucleus is also visible in our Hα + [N II] emission image of NGC 3898 (Fig. 13), mapping the ionized-gas distribution of the galaxy. The ionized-gas emission is smooth and featureless in the bulge-dominated region ($r \lesssim 20$ arcsec), where about 10 per cent of the warm gas resides. It shows a clumpy and fragmented distribution in the disc-dominated region where numerous H II regions trace the NGC 3898 multiple-arm structure. The transition between the two regions occurs abruptly at 35 arcsec from the centre, where the gas emission in the major-axis spectrum (Fig. 8) cuts off. The distribution of the H II regions (which closely follows the continuum isophotes) indicates that the gas and stellar discs are coplanar.

On the SW side of the galaxy, two series of emission knots are aligned at projected angular distances of 80 and 180 arcsec from the centre, respectively (Fig. 14). These H II regions trace the two external faint arms located far beyond the galaxy, main body of the as discussed in the Carnegie Atlas of Galaxies (Sandage & Bedke 1994, panel 79).

5.2.4 *Dynamical modelling*

In Fig. 15 we show the comparison between the photometric and kinematic data and the best-fitting dynamical model obtained with the technique discussed in Section 4.2. The mass-to-light ratios of the bulge and disc stellar component are shown in Table 14.

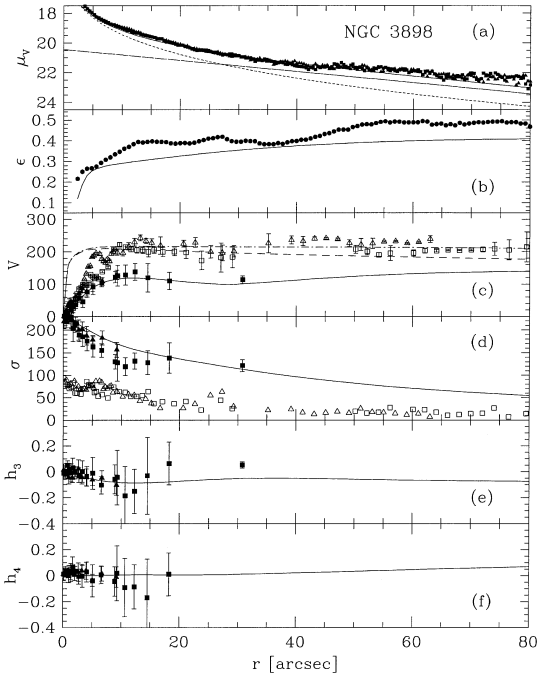

Figure 15. Same as Fig. 7, but for NGC 3898. The *squares* and *triangles* represent data measured on the receding SE and approaching NW sides, respectively. In panel (c) the model circular velocity is plotted with (*dot-dashed line*) and without (*dashed line*) the contribution of a dark matter halo with the structural parameters given in Table 14.

A number of kinematic features highlight the presence of a hot spheroidal component. At $|r| = 12$ arcsec both h_3 and h_4 show the presence of a non-Gaussian LOSVD, which can be interpreted as due to the superposition of a radiply rotating disk and an almost non-rotating bulge. The stellar rotation velocity is everywhere less than $2/3$ of the gas velocity, as a result of the asymmetric drift effect. Finally, for $12 \lesssim |r| \lesssim 25$ arcsec the stellar velocity dispersion shows a plateau at a value of $110\,\mathrm{km\,s^{-1}}$, which is the signature of a thick, dynamically hot component.

The gas rotation velocity is well approximated by the circular velocity of our models for $|r| > 8$ arcsec. Out to 80 arcsec from the centre, the gas rotation curve does not show hints of an asymmetric drift effect, and is almost flat at the constant value of about $200\,\mathrm{km\,s^{-1}}$. Kent (1988) and Moriondo et al. (1998b) already pointed out that for $|r| \lesssim 8$ arcsec the gas rotates more slowly than expected on the basis of the stellar kinematics and of the photometry. The comparison of the observed gas kinematics with our self-consistent dynamical model confirms this result. Moreover, we can also conclude that seeing convolution and finite slit width can not account for this effect, since these parameters were already included in the computation of our modelled velocity curves. We stress that, for this particular object, the gas rotation curve can not be interpreted as a sign of 'pressure-supported' gas in the central regions of the galaxy. First, the observed gas velocity dispersion is too low to account for the large differences between the circular velocity computed from the model and the observed gas rotation velocity. Moreover, the gas kinematics show strong asymmetries in the region where the 'slowly rising' effect takes place, with a difference of more than $80\,\mathrm{km\,s^{-1}}$ in the rotation velocities of the leading and receding sides. Such asymmetries are not seen in the gas velocity-dispersion profile. It is likely that other effects are at work here; however, the available data do not allow us to distinguish between non-axisymmetric distortion of a gaseous disc and possible non-equilibrium motions of the gas.

For this galaxy only we were not able to reproduce the gas rotation velocities at large radii without adding a dark matter halo. For sake of simplicity, we adopted the 'maximum bulge + disc' paradigm, in order to minimize the amount of dark matter needed to fit the data. A more precise measurement of the mass and distribution of the dark matter would require a best-fitting procedure of the observed kinematic curves varying simultaneously all the parameters involved, but can not be applied to this object because of the limited extension of the gas rotation curve ($\approx 2h$; see Persic, Salucci & Stel 1996 for a discussion on the subject). We assumed a pseudo-isothermal profile for the dark halo with a circular velocity, given by

$$V_\mathrm{c}^2(r) = v_\mathrm{h}^2\left[1 - \frac{r_\mathrm{h}}{r}\arctan\left(\frac{r}{r_\mathrm{h}}\right)\right] \qquad (12)$$

Due to the limitations of the available data, we were unable to determine both the total mass and scale radius of the halo. Nevertheless, the total mass *within* the outermost observed radius was quite well constrained and turned out to be $9 \times 10^9\,\mathrm{M_\odot}$, with an error of less than 10 per cent. We also found that the scalelength of the dark halo is so large ($r_\mathrm{h} > 65$ arcsec), that in the observed radial range the circular velocity contributed by the halo rises almost linearly with radius.

Total mass estimates and mass decompositions for this galaxy are already present in literature (Fillmore et al. 1986; Kent 1998; Moriondo et al. 1998b). Remarkably, despite the various different hypotheses adopted, our result for the total luminous mass agrees within 20 per cent with all these authors: when scaled to our adopted distance of $D = 17.1$ Mpc, Kent (1988) gives $M_\mathrm{lum} = 1.1 \times 10^{11}\,\mathrm{M_\odot}$, Fillmore et al. (1986) $M_\mathrm{lum} = 1.1 \times 10^{11}\,\mathrm{M_\odot}$, and the most recent estimate, given by Moriondo et al. (1998b) is $M_\mathrm{lum} = 9.2 \times 10^{10}\,\mathrm{M_\odot}$, almost identical to our value of $M_\mathrm{lum} = 9.1 \times 10^{10}\,\mathrm{M_\odot}$. On the contrary, the mass decomposition of the different authors differs from each other by large factors, being strongly dependent on the hypothesis adopted. Kent (1988) and Moriondo et al. (1998b) derive bulge masses, which are respectively 15 and 3 times lower than the value we obtained. This is due to their assumption that the gas rotation velocities were tracing the potential everywhere. As a consequence, unphysical values for the mass-to-light ratios of both components are found, as the authors correctly remarked. This underestimate of the bulge contribution to the total mass content leads also to an overestimate the disc mass (by a factor of 4, if compared with our results) and the mass of the dark halo (in the case of Moriondo et al. 1998b).

Fillmore et al. (1986) derived the mass-to-light ratios from the stellar kinematics rather than from the gas; however, their photometric decomposition is one-dimensional and leads to a smaller and more compact bulge in combination with a larger disc than the ones we derived. Therefore their results are not easily comparable with ours. On the other hand, our two-dimensional photometric decomposition give a bulge-to-disc ratio in good agreement with both Kent (1988) and Moriondo et al. (1998b), who did not use for their decomposition the ellipse-averaged surface-brightness profiles as done by Fillmore et al. (1986).

5.3 NGC 7782

5.3.1 Stellar and ionized-gas kinematics

The stellar velocity curve is observed out to 40 arcsec (14.6 kpc)

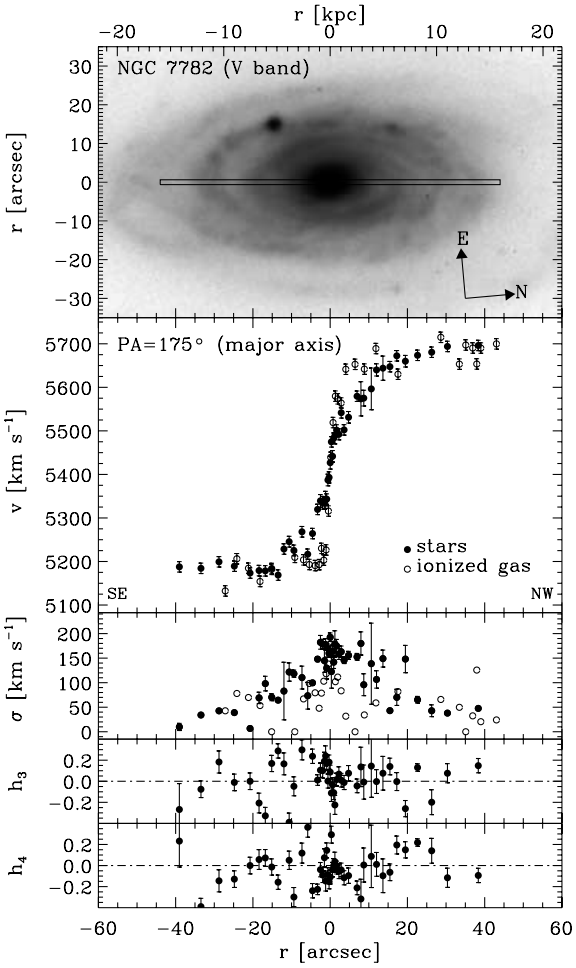

Figure 16. The stellar (*filled circles*) and ionized-gas (*open circles*) kinematic parameters measured along the major axis (PA = 175°) of NGC 7782.

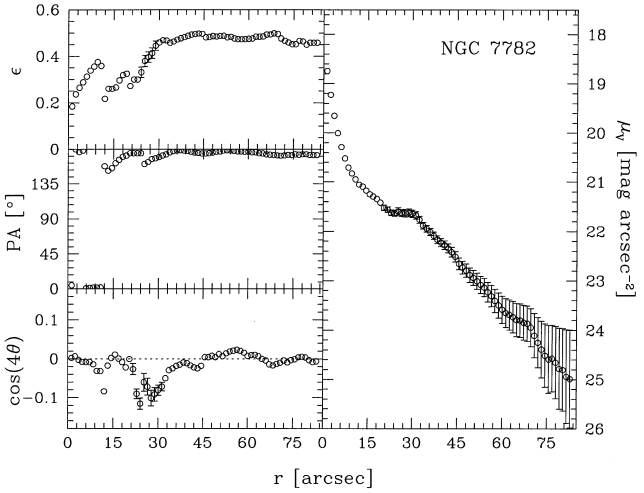

Figure 17. The *V*-band surface-brightness, ellipticity, position angle and $\cos 4\theta$ coefficient profiles as function of the semimajor axis length for NGC 7782. Error bars smaller than symbols are not plotted.

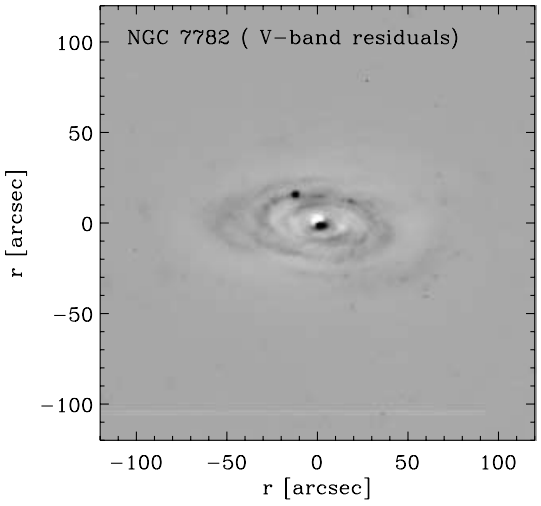

Figure 18. The residual image of NGC 7782 obtained by subtracting the model surface brightness from the observed one. The orientation of the image is the same as that of Fig. 16. The photometric parameters of the model are given in Table 13.

on both sides of NGC 7782 (Fig. 16). The stellar rotation velocity increases linearly up to 70 km s^{-1} in the inner 1 arcsec (0.4 kpc). It does not change for $1 \lesssim |r| \lesssim 3$ arcsec (1.1 kpc), and further out it shows a shallower gradient rising to 240 km s^{-1} at 14 arcsec (5.1 kpc). Outwards, the stellar rotation velocity remains constant or possibly even rises. At the centre the stellar velocity dispersion peaks to about 190 km s^{-1}, then off the nucleus it decreases gradually to less than 50 km s^{-1} at the last outermost radii.

The ionized-gas velocity curve extends to less than 30 arcsec (10.9 kpc) on the approaching side and to less than 45 arcsec (16.4 kpc) on the receding side of the galaxy (Fig. 16). The gas rotation velocity has a steeper gradient than the stellar curve, rising to 240 km s^{-1} at 3 arcsec; then it remains almost constant, becoming similar to the stellar velocity for $|r| > 14$ arcsec. The gas velocity dispersion is centrally peaked at about 180 km s^{-1}, dropping to values lower than 100 km s^{-1} for radii larger than 3 arcsec on both sides of the galaxy. Further out, it oscillates around values of about 40 km s^{-1}. The gas velocity dispersion is not greater than the stellar dispersion over the whole observed radial range.

5.3.2 *V-band surface photometry and bulge–disc decomposition*

The *V*-band radial profiles of surface brightness, ellipticity, position angle and $\cos 4\theta$ Fourier coefficient of NGC 7782 are measured out to 83 arcsec (30.3 kpc) from the centre (Fig. 17).

The ellipticity increases from 0.18 to 0.37 in the first 10 arcsec (3.6 kpc), dropping to 0.22 further out. It then increases again to 0.48, and flattens around this value for $r \geq 30$ arcsec. The position angle is constant at 175° at almost all radii, except for two abrupt changes at 6 and 18 arcsec by less than 20°. Isophotes are boxy-shaped around 6 arcsec and between 18 and 36 arcsec, and almost elliptical elsewhere. The surface-brightness profile is characterized by a plateau at 21.6 mag arcsec^{-2} between 23 and 30 arcsec. All these features can be explained as due to the spiral pattern (see Fig. 18).

The *V*-band surface-brightness radial profile of Kodaira et al. (1990) has been extracted along the galaxy major axis, but it is not directly comparable with the ellipse-averaged one we have derived and shown in Fig. 17.

The two-dimensional bulge–disc parametric decomposition of NGC 7782 was performed, adopting an exponential bulge since

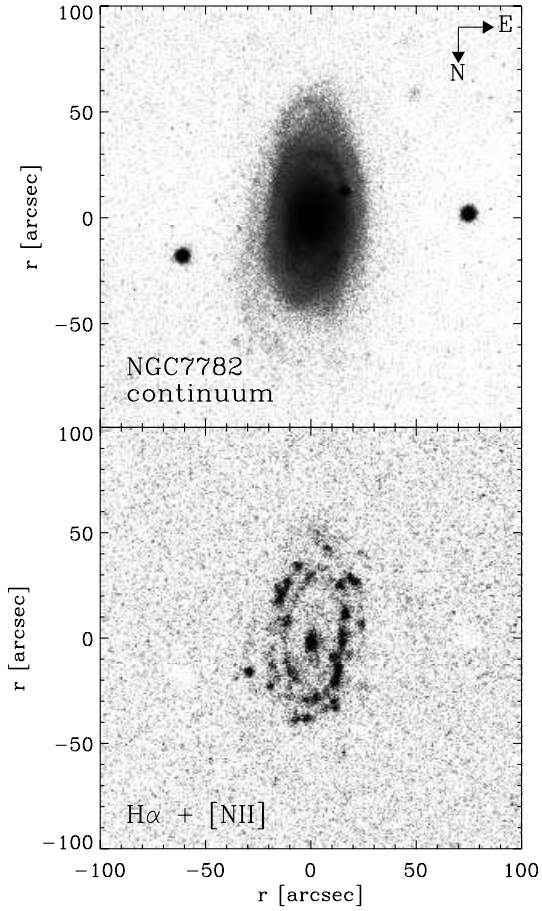

Figure 19. The stellar-continuum image (*upper panel*) and the continuum-subtracted Hα + [N II] emission image (*lower panel*) of NGC 7782.

this yielded lower residuals. The map of the residuals obtained as a difference between the observed and the model surface brightness is plotted in Fig. 18. This figure shows the asymmetric pattern of the inner stellar spiral arms.

5.3.3 *Ionized-gas distribution*

The ionized-gas distribution of NGC 7782 is shown in Fig. 19. The map of the Hα + [N II] emission is characterized by the presence of a small and bright nuclear region aligned with the galaxy major axis, and two tightly wound spiral arms which can be followed for 360°, forming a sort of double ring-like structure. The gaseous arms are more symmetric than the stellar arms and do not extend to the inner region of the galaxy, starting outside the constant surface-brightness region at 30 arcsec from the centre.

As in the case of NGC 772, the bright Hα + [N II] nucleus of NGC 7782 is characterized by a high ionized-gas velocity dispersion ($\sigma_{\rm gas} > 100\,{\rm km\,s^{-1}}$ for $|r| \lesssim 3$ arcsec) as shown in Fig. 16, suggesting the possible presence of pressure-supported gas in the bulge region. In spite of its apparent clumpy distribution (Fig. 19), a diffuse component of ionized gas is also present in the disc of NGC 7782, as indicated by the fact that we are able to measure continuously the ionized-gas velocity parameter without gaps along the complete major axis out to 30 and 45 arcsec on the two sides of the nucleus (Fig. 16), respectively. The distribution of the H II regions, following the continuum isophotes, indicates that the gas and stellar discs are coplanar.

5.3.4 *Dynamical modelling*

The comparison between the photometric and kinematic data and the best-fittting photometric dynamical models we obtained for NGC 7782 is shown in Fig. 20. The mass-to-light ratios, the flattening and the masses of the bulge and disc stellar components derived using the dynamical modelling technique described in Section 4.2 are given in Table 14.

From both the kinematic and the photometric data shown in Fig. 20 we can clearly distinguish the bulge- and disc-dominated regions.

An exponential and almost spherical bulge is the main photometric and dynamical component within 4 arcsec from the centre. In this region the stellar velocity dispersion shows a plateau at $180\,{\rm km\,s^{-1}}$ and, in agreement with the asymmetric drift effect calculated by the model, the stellar rotation velocity is below the value of the circular velocity. In the transition region $2 \lesssim |r| \lesssim 7$ arcsec the gas rotation curve shows small deviations ($|V_{\rm gas} - V_{\rm circ}| \lesssim 50\,{\rm km\,s^{-1}}$) from pure circular rotation. Any evidence for possible non-circular motions is marginal, and the increase of the gas velocity dispersion towards the nucleus can be better explained as due to a seeing effect.

For $|r| > 15$ arcsec the surface brightness and ellipticity profiles of NGC 7782 are dominated by the light contribution of the disc component. Therefore in the outer region, asymmetric drift effect is negligible, and both gas and stars appear to rotate close to the circular velocity. No dark matter halo is required to reproduced the observed velocity curve out to the last observed radius.

Since the h_3 and h_4 values are poorly constrained by observations, it is not possible to draw any conclusion about anisotropies in the stellar velocity dispersion.

6 DISCUSSION AND CONCLUSIONS

Non-circular velocities of the ionized gas in the bulge-dominated region of early-to-intermediate-type disc galaxies have been detected by different authors (Fillmore et al. 1986; Kent 1988; Kormendy & Westpfahl 1989). The discovery that in a large fraction of S0s galaxies the gas velocity dispersion remains as high as the stellar velocity dispersion over an extended radial range (Bertola et al. 1995) corroborated the early suggestions that at small radii gas could be dynamically hot rather than settled in a cold disc. In this framework, the dynamical modelling by Cinzano et al. (1999) showed that in the S0 galaxy NGC 4036 the difference between the circular velocity curve inferred from stellar kinematics and the rotation curve of the gas is substantially accounted for its high velocity dispersion.

It is usually customary, in measuring mass distribution, to assume that the ionized gas is moving in circular orbits. It is therefore crucial to understand if and when the warm gas in galaxies has a rotation curve which rises more slowly than the gravitational equilibrium circular velocity. Ignoring this effect can lead to a significant underestimate of the masses of the bulge, disc and dark halo (see, e.g., Kent 1988 for a discussion). Up to now such a direct comparison between the circular velocity inferred from dynamical modelling based on stellar kinematics and surface photometry and the observed gas rotation velocity has been made for only a small set of lenticulars and early-to-intermediate spirals (see Table 15). The three new cases discussed in this paper therefore represent a useful step in understanding how common

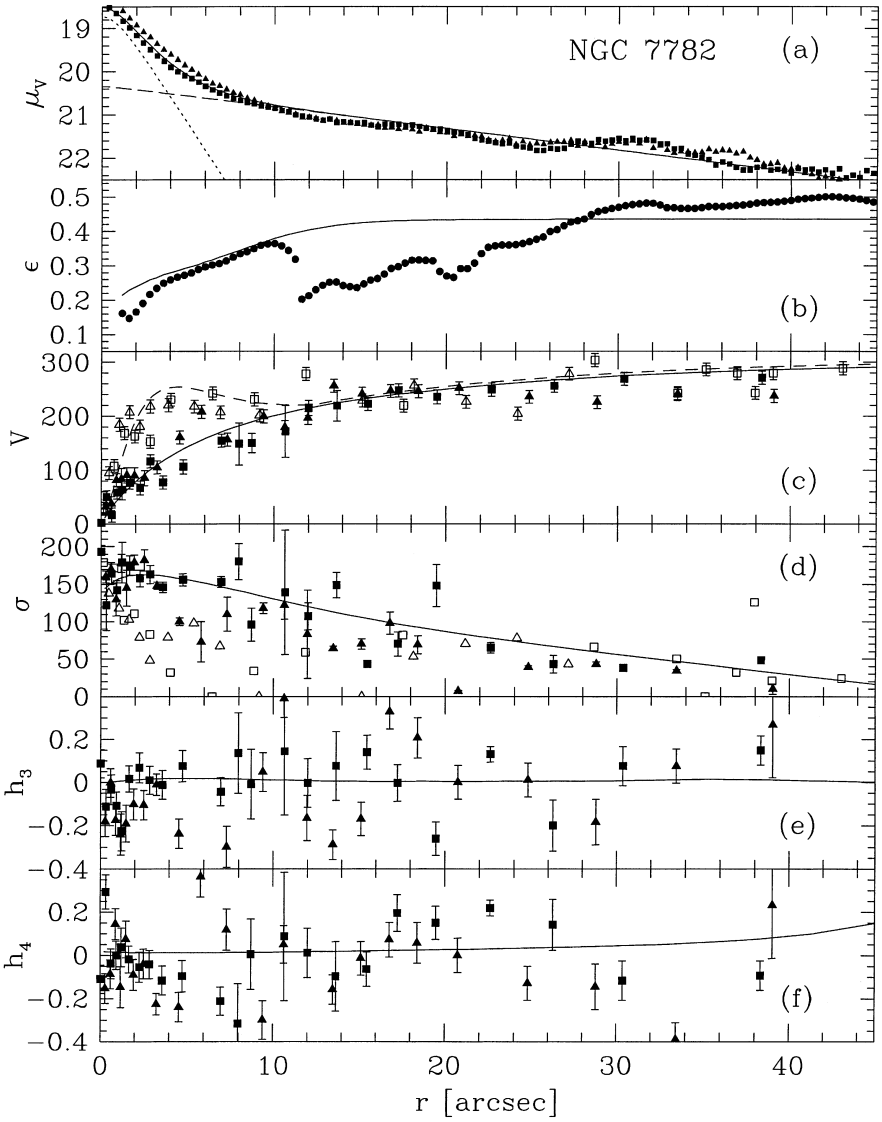

Figure 20. Same as Fig. 7, but for NGC 7782. The *squares* and *triangles* represent data measured on the receding NW and approaching SE sides, respectively.

the phenomenon of slowly rising rotation curves is in bulge-dominated galaxies.

For NGC 772, 3898 and 7782 we present a self-consistent Jeans model for the stellar kinematics, adopting the light distribution of bulge and disc derived by means of a two-dimensional parametric photometric decomposition of the observed *V*-band surface brightness. This allows us not only to investigate the presence of non-circular gas motions, but also to derive the mass distribution of luminous and dark matter in these objects.

In NGC 772 the observed velocity dispersion of the ionized gas is comparable to the stellar velocity dispersion and is far higher than expected from the thermal motions or small-scale turbulence, typically observed in a gaseous disc. However, dynamical modelling showed that the rotation of the ionized gas traces the circular velocity and that the central rise observed in its velocity dispersion is due to seeing effects, which serves as a warning against over-interpretation.

On the contrary, the gas rotation curve of NGC 3898 can be classified as 'slowly rising', since for the inner 8 arcsec the ionized gas is rotating more slowly than the circular velocity predicted by dynamical modelling. NGC 3898 is the only galaxy of our sample for which previous determinations of the masses of the bulge and disc components are available in the literature (Fillmore et al. 1986; Kent 1988; Moriondo et al. 1998b). Comparison shows that NGC 3898 is a clear-cut example that mass decomposition based only on emission-line rotation curves can be unreliable, at least for bulge-dominated galaxies. This error was made and discussed by Kent (1988) and Moriondo et al. (1998b), who assumed the gas to be rotating at circular velocity at all radii and found extraordinarily low values for the mass-to-light ratio of the spheroidal component, as if NGC 3898 was an almost 'bulgeless' galaxy in spite of its overall morphology (see Table 1 and Figs 8 and 13) and bulge-to-disc luminosity ratio ($B/D = 2$). The asymmetry of the gas rotation curve of NGC 3898 (with a maximum ΔV between the two sides of about $80\,\mathrm{km\,s^{-1}}$ at 6 arcsec from the centre), and the strong difference between the gas ($\sigma_{\rm gas} \leq 90\,\mathrm{km\,s^{-1}}$) and the stellar velocity dispersion ($\sigma_{\rm stars} > 120\,\mathrm{km\,s^{-1}}$ with a central peak to $210\,\mathrm{km\,s^{-1}}$) in the innermost 5 arcsec (where we observe almost the same velocity gradient for both gas and stars) are an indication that along with random

Table 15. Early-to-intermediate type disc galaxies with available comparison between gas rotation velocity and circular speed.

Object	Morphological Type [RSA]	[RC3]	D [Mpc]	$M^0_{B_T}$ [mag]	$M_{\rm bulge}/M_{\rm disc}$	$r_{\rm e}$ [kpc]	r_μ [kpc]	$V_{\rm gas} < V_{\rm circ}$	r_V [kpc]	r_σ [kpc]	Ref.
(1)	(2)	(3)	(4)	(5)	(6)	(7)	(8)	(9)	(10)	(11)	(12)
NGC 772	Sb(rs)I	.SAS3..	34.7	−21.61	2.11	11.0	6.2	no	–	0.5	1, *V*
NGC 2179	Sa	.SAS0..	33.7	−19.81	2.80	2.0	5.7	no	–	0.2	2, *R*
NGC 2775	Sa(r)	.SAR2..	13.9	−19.91	1.39	3.6	4.4	yes	2.0	–	2, *r*
NGC 3898	SaI	.SAS2..	17.1	−19.84	3.55	1.6	2.3	yes	0.7	–	1, *V*
NGC 4036	$S0_3(8)$/Sa	.L..–..	20.1	−20.03	2.04	1.2	0.7	yes	1.0	0.4	3, *V*
NGC 4450	Sab pec	.SAS2.	17.0	−20.40	2.69	1.7	1.4	yes	>5.0	?	4, *B*
NGC 4569	Sab(s)I-II	.SXT2..	17.0	−21.36	0.08	0.3	0.4	yes	2.6	?	4, *B*
NGC 5055	Sbc(s)II-III	.SAT4..	7.5	−20.35	0.12	0.4	0.3	yes	0.5	?	4, *B*
NGC 7782	Sb(s)I-II	.SAS3..	74.8	−21.95	0.24	1.1	1.5	no	–	0.4	1, *V*

NOTE – col. 2: morphological type from RSA; col. 3: morphological type from RC3; col. 4: distance derived as V_0/H_0, with V_0 the velocity relative to the centroid of the Local Group obtained from the heliocentric systemic velocity as in RSA and $H_0 = 75\,{\rm km\,s^{-1}\,Mpc^{-1}}$. The heliocentric velocity of NGC 5055 has been taken from RC3. For NGC 4450 and 4569, which belong to the Virgo cluster, the distance has been taken following Freedman et al. (1994); col. 5: absolute corrected B magnitude from B^0_T in RC3; col. 6: bulge-to-disc mass ratio; col. 7: effective radius of the $r^{1/4}$ bulge. For NGC 7782 the bulge has an exponential surface-brightness profile; col. 8: radius at which $\mu_{\rm bulge} = \mu_{\rm disc}$; col. 9: yes = the ionized-gas component shows a slowly rising rotation curve (i.e., $V_{\rm gas} < V_{\rm circ}$ at small radii), no = the gas rotation traces circular speed at all radii ($V_{\rm gas} = V_{\rm circ}$ at all radii); col. 10: radial range in which $V_{\rm gas} < V_{\rm circ}$; col. 11: radial range in which $\sigma_{\rm gas} \simeq \sigma_{\rm stars}$, ? = the radial profile of the ionized-gas velocity dispersion is not available; col. 12: references and bands of the data [1 = this paper, 2 = Corsini et al. (1999), 3 = Cinzano et al. (1999), 4 = Fillmore et al. (1986)].

motions other phenomena could also be contributing to the slow rise of the gas velocity. This is the case for other galaxies with slowly rising rotation curves, such as the Sa galaxy NGC 2775 (Corsini et al. 1999) and the S0 galaxy NGC 4036 (Cinzano et al. 1999). The asymmetry of the inner parts of the gas rotation curve of NGC 2775 has been explained as due to a gaseous component which is not rotating in the galaxy plane, and the possible presence of drag forces between the ionized gas and the hot component of the interstellar medium of NGC 4036 has been suggested (for a discussion of the phenomenon see Cinzano et al. 1999).

Finally, in NGC 7782 the gas rotation curve shows small deviations from pure circular rotation only in the transition region between bulge and disc. Any evidence for possible non-circular motions is marginal, and the sharp increase of the gas velocity dispersion towards the nucleus can be better explained as due to a seeing effect, as in the case of NGC 772.

As far as the presence of dark matter is concerned, we infer that the mass is essentially traced by light in NGC 772 and 7782, where gas rotation velocities were observed out to $0.2R_{25}$ and $0.6R_{25}$, respectively. For NGC 3898 the combined stellar and gaseous rotation data (which extend out to $0.2R_{25}$ and $0.7R_{25}$, respectively) require the presence of a massive dark halo. This result is based on the idea that gas kinematics at large radii is representative of a dynamically cold disc supported by rotation, as suggested by the high gas rotation velocity and low velocity dispersion ($V/\sigma \simeq 10$) for $r > 30$ arcsec (corresponding to about $0.2R_{25}$). This result also qualitatively agrees with the general dark matter scenario, with the less massive galaxies being the more dark-matter-dominated (Salucci & Persic 1999), although these data do not permit a careful measurement of the dark halo properties.

Kent (1988) found that, out of the 14 Sa galaxies he modelled, six show gas rotation curves that rise too slowly for a constant mass-to-light ratio, implying that they are respectively too low for the bulges and too high for the disc components. According to Table 15, the gas motion is not circular in the inner regions of six of the nine early-to-intermediate disc galaxies, for which dynamical modelling allows a direct comparison between the gaseous and circular speeds (among these only NGC 3898 belongs also to Kent's sample).

Without pretending to draw any statistical conclusion based on so small a number of objects, it nevertheless seems probable that non-circular gas velocities could be a common feature in the central kiloparsec of disc galaxies ranging from S0s to Sbs. However, according to the available data, it is not possible to derive a straightforward correlation with the galaxy morphological type, total luminosity, bulge-to-disc mass ratio or bulge size. It seems that even if the gas may be supported by non-circular random motions, this type of dynamical-pressure support may not be the only effect for the 'slowly rising' gas rotation curves. In fact, the central gas velocity dispersion is too low to account for the difference between gas and circular speeds in two of the three galaxies (namely NGC 2775 and 3898) shown in Table 15, for which the gas velocity falls short of the circular speed and the velocity-dispersion profile of the gaseous component is available. Dynamical modelling based both on stellar and gaseous kinematics of a larger number of bulge-dominated galaxies is needed to understand the links between slowly rotating gas and bulge properties, as a first step to put constraints on their physical nature (e.g. Mathews 1990) and origin (e.g. Bertola et al. 1995).

ACKNOWLEDGMENTS

We are grateful to Prof. P. A Strittmatter, Director of the Steward Observatory, and to Dr G. V. Coyne, S. J., Director of the Vatican Observatory, for the allocation of time for our observations. WWZ acknowledges the support of the grant 7914 of the *Jubiläumsfonds der Oesterreichischen Nationalbank*. This work was partially supported by grant PB97-0214 of the Spanish DGES. This paper was based on observations carried out at the Multiple Mirror Telescope Observatory (Arizona, USA), which is a joint facility of the Smithsonian Institution and the University of Arizona, with the Isaac Newton Telescope, which is operated on the island of La Palma by the Isaac Newton Group in the Spanish Observatorio del Roque de los Muchachos of the Instituto de Astrofísica de Canarias, and with the Vatican Advanced Technology Telescope, which is the Alice P. Lennon Telescope and the Thomas J. Bannan Astrophysics Facility at the Mount Graham International Observatory (Arizona, USA).

REFERENCES

Baggett W. E., Baggett S. M., Anderson K. S. J., 1998, AJ, 116, 1626
Barbon R., Benacchio L., Capaccioli M., 1978, A&A, 65, 165
Bender R., 1990, A&A, 229, 441
Bender R., Saglia R. P., Gerhard O. E., 1994, MNRAS, 269, 785
Bertola F., Corsini E. M., 1999, in Barnes J. E., Sanders D. B., eds, Proc. IAU Symp. 186, Galaxy Interactions at Low and High Redshift. Kluwer, Dordrecht, p. 149
Bertola F., Cinzano P., Corsini E. M., Rix H.-W., Zeilinger W. W., 1995, ApJ, 448, L13
Bettoni D., Galletta G., 1997, A&AS, 124, 61
Bevington P. R., Robinson D. K., 1992, Data Reduction and Error Analysis for the Physical Sciences. McGraw-Hill, New York
Binney J., Merrifield M., 1998, Galactic Astronomy. Princeton Univ. Press, Princeton
Boroson T., 1981, ApJS, 46, 177
Burstein D., 1979, ApJ, 234, 435
Byun Y. I., Freeman K. C., 1995, ApJ, 448, 563
Carollo C. M., Stiavelli M., de Zeeuw P. T., Mack J., 1997, AJ, 114, 2366
Carollo C. M., Stiavelli M., Mack J., 1998, AJ, 116, 68
Cinzano P., Rix H.-W., Sarzi M., Corsini E. M., Zeilinger W. W., Bertola F., 1999, MNRAS, 307, 433
Corsini E. M., et al., 1999, A&A, 342, 671
Courteau S., 1996, ApJS, 103, 363
de Vaucouleurs G., 1948, Annales d'Astrophysique, 11, 247
de Vaucouleurs G., de Vaucouleurs A., Corwin H. G., Jr, Buta R. J., Paturel G., Fouqué P., 1991, Third Reference Catalogue of Bright Galaxies. Springer-Verlag, New York (RC3)
Fillmore J. A., Boroson T. A., Dressler A., 1986, ApJ, 302, 208
Fisher D., 1997, AJ, 113, 950
Freedman W. L. et al., 1994, Nat, 371, 757
Freeman K. C., 1970, ApJ, 160, 811
Friedli D., 1996, A&A, 312, 761
Giovanardi C., Hunt L. K., 1996, AJ, 111, 1086
Guthrie B. N. G., 1992, A&AS, 93, 255
Heraudeau P., Simien F., 1996, A&AS, 118, 111
Heraudeau P., Simien F., 1998, A&AS, 133, 317
Heraudeau P., Simien F., Maubon G., Prugniel P., 1999, A&AS, 136, 509
Ho L. C., Filippenko A. V., Sargent W. L. W., 1997, ApJS, 112, 315
Jedrzejewky R. I., 1987, MNRAS, 226, 747
Kent S. M., 1985, ApJS, 59, 115
Kent S. M., 1988, AJ, 96, 514
Kodaira K., Okamura S., Ichikawa S.-I., 1990, Photometric Atlas of Northern Bright Galaxies. Univ. Tokyo Press, Tokyo
Kormendy J., Westpfahl D. J., 1989, ApJ, 338, 752
Krumm N., Salpeter E. E., 1980, AJ, 85, 1312
Lu N. Y., 1998, ApJ, 506, 673
Mathews W. G., 1990, ApJ, 354, 468
Moriondo G., Giovanardi C., Hunt L. K., 1998a, A&AS, 130, 81
Moriondo G., Giovanardi C., Hunt L. K., 1998b, A&A, 339, 409
Moriondo G. et al., 1999, A&AS, 137, 101
Moshir M. et al., 1990, Infrared Astronomical Satellite Faint Source Catalogue, Version 2.0
Nilson P., 1973, Uppsala General Catalogue of Galaxies. Royal Society of Sciencies of Uppsala, Uppsala (UGC)
Persic M., Salucci P., Stel F., 1996, MNRAS, 283, 1102
Pignatelli E., Galletta G., 1999, A&A, 349, 369
Press W. H., Teukolsky S. A., Vetterling W. T., Flannery B. P., 1996, Numerical Recipes in Fortran 77: The Art of Scientific Computing. Cambridge Univ. Press, Cambridge
Rhee M.-H., van Albada T. S., 1996, A&AS, 115, 407
Rubin V. C., Burstein D., Ford W. K., Jr, Thonnard N., 1985, ApJ, 289, 81
Salucci P., Persic M., 1999, A&A, 351, 442
Sandage A., Bedke J., 1994, The Carnegie Atlas of Galaxies. Carnegie Institution and Flintridge Foundation, Washington
Sandage A., Tammann G. A., 1981, A Revised Shapley-Ames Catalog of Bright Galaxies. Carnegie Institution, Washington (RSA)
Schombert J. M., Bothun G. D., 1987, AJ, 93, 60
Simien F., de Vaucouleurs G., 1986, ApJ, 302, 564
Sofue Y., Rubin V. C., 2001, ARA&A, 39, submitted (astro-ph/0010594)
van Albada T. S., Sancisi R., 1986, Royal Society of London Philosophical Transactions Series, 320, 447
van der Marel R. P., Franx M., 1993, ApJ, 407, 525
van Driel W., van Woerden H., 1994, A&A, 286, 395
Vega Beltrán J. C., 1999, PhD thesis, Instituto de Astrofísica de Canarias
Wadadekar Y., Robbason B., Kembhavi A., 1999, AJ, 117, 1219
Watanabe M., 1983, Annales of the Tokyo Astronomical Observatory, 19, 121
Whitmore B. C., Rubin V. C., Ford W. K.,Jr. 1984, ApJ, 287, 66
Young J. S., Xie S., Kenney J. P. D., Rice W. L., 1989, ApJS, 70, 699

This paper has been typeset from a TEX/LATEX file prepared by the author.